An in depth boundary region study of the zodiacal cloud in the inner heliosphere

by

Alexandru Toma

A thesis submitted to the

Faculty of the Physics Department at the

University of Colorado in partial fulfillment

of the requirements for the degree of

Bachelor of Arts in Physics

Department of Physics

April 7 2023

Committee Members:

Dr. David Malaspina, Thesis Advisor, Department of Astrophysical 7 Planetary Sciences

Dr. Michael Ritzwoller, Honors Council Representative, Department of Physics

Dr. Steven Pollock, Outside Reader, Department of Physics

Toma, Alexandru (BA., Physics)

An in depth boundary region study of the zodiacal cloud in the inner heliosphere

Thesis directed by Prof. Dr. David Malaspina, Thesis Advisor, Department of Astrophysical 7
    Planetary Sciences

The shape of the zodiacal cloud and the process by which planets are formed comes from direct interstellar dust interaction with a nearby star. This occurs at a close distance labeled the inner heliosphere (radius $\leq$ 20 AU). The *Parker Solar Probe* mission has the ability to detect interplanetary dust in-situ in the inner heliosphere region, using voltage pulses measured by the FIELDS instrument. Voltage pulses are the byproduct of dust impacting the spacecraft represented by a plasma cloud. These dust observations give us insight into near stellar dust dynamics and characteristics. A model of the dust density near the sun has been created by PSP's Wide Field Imager (WISPER) team. Using white-light images of the region up to $7.5R_\odot$ and looking at changes in the radial gradient of the brightness profile, they were able to characterize a dust depletion zone (DDZ). They observe the DDZ extends to $19R_\odot$. Closer to the sun ($3R_\odot$) they define a dust free zone (DFZ) where there are no dust particles present. The model developed by WISPR is developed through remote sensing and needs to be compared to in-situ measurements to verify the validity of the model. This is one of the main goals of the WISPR instrument. In an effort to produce a Inner Heliosphere Dust Model, we created an in-situ database of dust flux hitting the spacecraft using FIELDS voltage peak detection data (TDSmax). In the current work, we extend that database over all 13 encounters. Examining FIELDS burst data (high cadence time series antenna voltages), it is found that dust impacts may occur faster than the TDSmax data can register them. This can lead to an under-estimation of the dust flux. We constructed a database of dust impact observations from all FIELDS burst data. This burst database was used to analyze the probability of observing closely spaced impacts. Initial analysis shows that the probability distribution of these impacts is not Poisson in nature, but does have a clear radial dependence. These results are directly applied

as an empirical correction to the estimated dust flux. The corrected dust flux will be used to test the WISPR team's model. Additionally, we developed another method of correction involving the waiting time between impacts. This allowed us to use in-situ data to verify the outer boundary and structure of the DDZ, as well as allow us to make a more accurate prediction of the start of the DFZ. Initial observations of DDZ modeling using in situ measurements confirm its existence in the region. The start of the DDZ occurs at approximately $19R_\odot$.

Dedication

I want to dedicate this paper firstly to my parents: Elena and Ilie. Over the last 22 years they have worked hard to make sure that I am going into the world as a human capable of achieving anything I set my mind to. They both believed from the start that I was able to succeeded as a physicist. Their continued support and limit-breaking pushing towards achieving my goals in physics has allowed me to make sure that I am able to succeeded in the world of academia. Thank you for all you have done.

To my good friend and mentor George Rhee, who guided me on my early path towards physics and who still believes in the quest that I have set out on.

I would also like to dedicate this paper to myself as a freshman who came to the University of Colorado Boulder not knowing anything about physics and its intricate world. Who's timidness wasn't a weakness in his pursuit, but a stepping stone towards perseverance.

Acknowledgements

I would like to thank all the scientists and engineers who worked on making *Parker Solar Probe* a reality. The bedrock of solar dynamics and understanding could not have been possible if not for brilliant minds such as yours.

I would like to thank both the FIELDS and the WISPR who have given me the possibility to explore dust characteristics in space and who's work currently powers the intricate questions of our own solar system.

Thank you to Dr. Jamey R. Szalay of Princeton University, who's invaluable guidance and focus on team working has been an remarkable experience.

I would also like to thank the honors committee: Dr. David Malaspina, Dr. Michael Ritzwoller, and Dr. Steven Pollock for their hard work in reviewing and listening to my current work on stellar dust interactions with the sun.

Thank you to Dr. Malaspina's current grad students: Peter Tatum and Benjamin Short who have guided when I was lost and entertained my non-ending stream of questions regarding space physics research.

Finally I want to thank Dr. Malaspina himself, for giving me the chance to prove myself as a capable researcher in physics. His kindness, and willingness to always guide me has given the courage to further believe in my pursuit of academic research. Thank you for imparting onto me your wisdom, work ethic, rigor, and courage to go beyond the standard questioning an undergrad might experience in their career.

Contents

Chapter

Chapter 1

Introduction

People have always been curious about the qualities and composition of materials. People are naturally inclined to pick up a rock and study its shape, feel, the color so that they can categorize it accordingly. As scientific technology has progressed, the ability to look at ever smaller objects has become possible, and with that, we started looking at dust. The size of dust particles varies at the level of the micron scale, but the underlying questions are still the same: "What is it made of"? "What does it react with"? "How does it look"?

These specific characteristic questions are not new, nor are they questions that will disappear anytime soon. Dust particles have been analyzed on earth at small scales, but scientists have been curious as to how these studies extend into the greater unknown. Space is a region that was not well understood and inaccessible until the early 20th century. Being that the earth was made up of rocks, which in turn is made up of dust, scientists were eager to explore dust in space and see if there were any new questions to answer, in addition to the basic characteristics.

With the rise of space exploration in the early twentieth century, we have come to ask the same questions about the dust that is millions of miles away from us. These are simple questions, but they allow for a more in-depth exploration of the concept of dust. This is important for future engineers and scientists who wish to launch spacecraft into space, some of which might travel directly through dust clouds. In this calculation, one must understand the risks associated with such travel. For example, the *Wind* spacecraft suffered damage from what was more than likely dust impacts on two separate occasions (Malaspina et al., 2014). Similarly, other spacecraft have

also suffered similar damage, limiting the possibility of measurements taken during a mission's lifetime. Having a deeper understanding of dust and the interactions that occur within space, gives a chance at mitigating damage (see London and Early (2018) for further information regarding impact damage of spacecraft).

Additionally, there is a growing interest in exoplanet research. To understand the basics of exoplanet formation an understanding of interactions between dust particles and stars must be formed. Dust particles are important to study in the formation of planetary formation theory.

The sun is a powerhouse in fueling the imagination of many fundamental scientific questions about space. From how its light reaches us to how its position in space affects all that is around it, scientists have yet to scratch the surface of this behemoth box filled with questions. Additionally, one might ask what would happen if you put dust near the sun. How would this question bring about changes or similarities to the overall questions that have been asked since the beginning? These questions might shed light on planet formation theory. To look at this concept, let us look at the early twentieth century.

Henry Norris Russell originally proposed, through the Sun's spectral lines ((Russell, 1929); (Koschny et al., 2019)), that dust particles in space do not touch the sun, rather they reach a point where the sublimate. The early twentieth century was a time of limited data collection, with spectral light being the main possible way to accumulate a deeper understanding of the inner solar region. With the advent of space exploration, we have had missions such as: *STEREO*, *Voyagers 2*, and *Cassini* that began to tap into the study of interplanetary dust, but they all suffered from the same issue: none of them got close to the sun, until *Parker Solar Probe*.

Before *Parker Solar Probe* we must quickly acknowledge the Helios 1 and Helios 2 missions that occurred before, and their role in *Parker Solar Probe*. Helios 1 and 2 were launched by NASA in the '70s with the scope of getting as close to the sun to understand solar processes. Helios 1 would go on to achieve its closest perihelion of 0.3 AU and produce substantial results on micrometeorites in the region. The following Helios 2 mission had the same objective as Helios 1 but was able to get closer to the sun, with a perihelion of 0.29AU. Helios 2 further provided detail on cosmic dust

and characteristics of the inner heliosphere. These values are far greater than *Parker Solar Probe*'s closest perihelion of 0.05 AU, but both Helios 1 and 2 should be acknowledged as the blueprint for creating *Parker Solar Probe.*

Parker Solar Probe is NASA's third attempt to get as close as possible to the sun, given the possible material constraints. With this state-of-the-art spacecraft, we hope to gain more understanding of the solar wind and dust particles in that near solar region(Fox et al. 2014). The spacecraft itself houses a range of different sensors and detectors. The main instruments used for this experiment are FIELDS (Bale et al. 2016), which makes in-situ measurements of electromagnetic fields, and WISPER, a wide field imager that is located on the side of the probe (Fox et al. 2014).

One shortcoming of *Parker Solar Probe* is that it has no dedicated dust detector on it. To combat this, FIELDS offers the possibility of studying dust through direct collisions with the spacecraft. The byproduct of these collisions is plasma clouds that can be measured as a voltage spike with unique characteristics. These voltage signals can be interpreted as dust impacts, making dust analysis possible without a dedicated detector.

In the following study we will look at: what interstellar dust is, what the *Parker Solar Probe* mission aims to achieve, a technical dive into the measuring of dust impacts aboard the spacecraft, data error correction, and a comparison of the WISPR team model, which explores the inner heliosphere boundary conditions of the zodiacal cloud.

Chapter 2

Interplanetary Dust

Space is commonly described as a vacuum. However, space is a near-perfect vacuum, containing: cosmic rays, electromagnetic waves, plasma, and dust. Any object in space is directly affected by these factors. This study examines the existence of dust and its characteristics in the inner heliosphere region of our solar system through interactions with human-made objects (NASA missions).

This chapter provides background on interplanetary dust and explains the different populations of dust particles examined in this study.

2.1   Interplanetary Dust

Interplanetary dust is directly produced from asteroids and comets. When larger bodies approach the sun, they may shed particles by sublimation or collisions. The velocity and trajectory of the shed dust particles are mainly dependent on the two acting forces : (i) gravitational force, and (ii) radiation pressure (Koschny et al., 2019).

Particles that are larger than 100 μm, are dominated by the gravitational force and become bound to the sun in an elliptical or near-perfect circular orbit (Koschny et al., 2019). This is modeled by the gravitational force equation:

$$F_g = G \frac{m_{dust} M_{sun}}{r^2} \tag{2.1}$$

where G is the gravitational constant of 6.674×10^{-11} $m^3/kg \times s^2$, m_{dust} and M_{sun} are the masses

Typical IDPs include: (left) anhydrous aggregate CP-IDPs, (center) single mineral IDPs, and (right) compact, hydrous IDPs. The arrow in the frame points to a pyroxene whisker
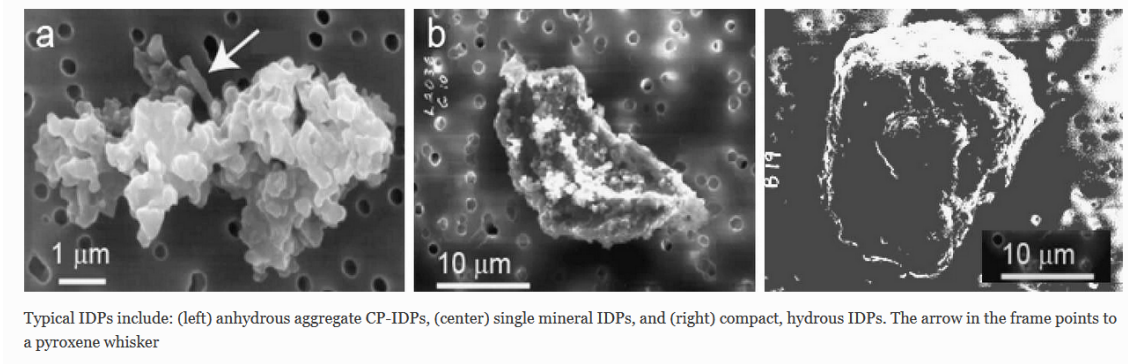
Figure 2.1: Examples of dust particles, with original description attached. (Koschny et al., 2019)

of the dust particle and the sun, and r represents the distance between the two bodies. In this study, these dust particles are labeled α-meteoroids.

Conversely, particles that are smaller than 100 μm are ejected on hyperbolic trajectories, because of the radiation pressure, resulting from momentum transfer produced by solar photons. particles like these are labeled in this study as β-meteoroids (Zook and Berg, 1975). β is a quantity that describes the ratio of the radiation pressure over the gravitational force as:

$$\beta = \frac{F_{radiation}}{F_g} = \frac{3L_\odot Q_{pr}}{16\pi G M_{sun} c \rho s} \tag{2.2}$$

where ρ is the mass density of the dust particle (measured quantity), $L_\odot$ is the Solar luminosity, s is the radius of our dust particle in m, c is the speed of light, and Q_{pr} represents the efficiency factor for radiation pressure (see (Koschny et al., 2019) and references therein).

There are additional, smaller, forces such as (i) Poynting-Roberston drag, (ii) Yarkovsky Effect, and (iii) Lorentz force. Poynting-Robertson drag is produced by the anisotropic radiation flux upon a particle moving at relativistic speeds. Acting as a drag force, it limits the time a dust particle spends in a bound orbit (Mann, 2009). The Yarkovsky effect is produced from anisotropically re-radiated photons from a rotating particle, but it is negligible for small particles. The Lorenz force applies to particles in a magnetic field. Similar to how point charges traveling through a magnetic field feel the Lorentz force, particles that travel through a magnetic field ($\mathbf{B}$),
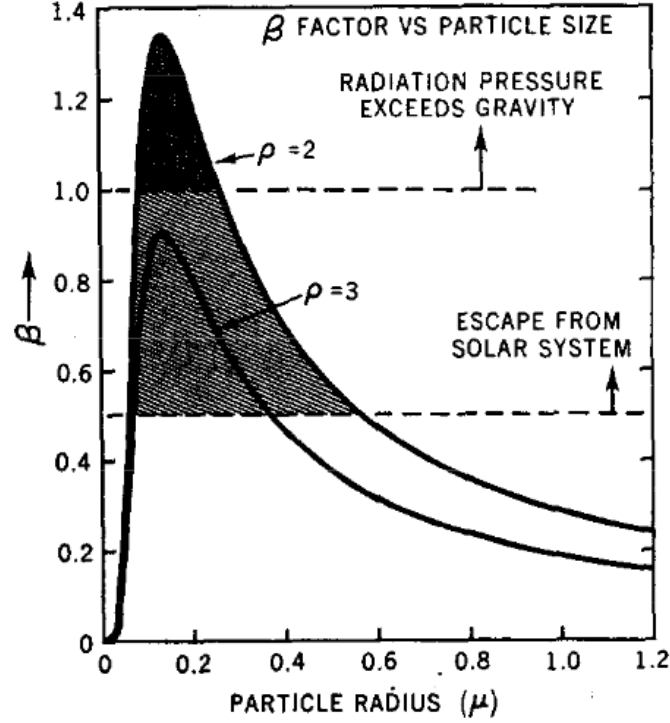
Figure 2.2: β values vs particle size. The ρ defines particle density. (Zook and Berg, 1975)

with a relative velocity ($\mathbf{v}_{rel}$) experience a force of:

$$F_{Lorentz} = \frac{q}{c}|\mathbf{v}_{rel} \times \mathbf{B}| \tag{2.3}$$

These forces change the motion of small dust particles, such that certain populations are driven sunward. As dust particles approach close to the sun other processes occur leading to particle destruction (Koschny et al., 2019).

2.2   Dust Free Zone Theory

In the early 20th century little was known about dust particles near the sun. Initial theories suggested that solid meteorites fell into the sun, however further research on the topic has shown that heavier particles composed of iron will disintegrate before reaching the sun. This process is known as sublimation. While heavy particles sublimate, it was still shown that the sublimated gas

eventually falls into the sun. A proposed region where no solid particles are present is called the Dust Free Zone (DFZ) (Russell, 1929).

The limitations of early 20th-century technology only allowed astronomers to study the inner heliosphere region using earth-based equipment. However, even later attempts such as (Mann 2004) yielded inconclusive results concerning the existence of the DFZ.

With recent NASA missions(*Parker Solar Probe*), capable of reaching extreme regions in our solar system, the possibility exists to explore near-sun space. This region is where interactions with the sun shape the dynamics and characteristics of the zodiacal cloud. We can now test previous theories using in-situ measurements.

Chapter 3

Parker Solar Probe

Parker Solar Probe (PSP) is an ongoing NASA mission that launched on August 12th, 2018, with the primary focus of exploring the near-sun environment. The mission has 24 planned orbits over a 7-year span. Gravitational assists from Venus help the spacecraft achieve a closer perihelion, with the closest being around $9R_\odot$.
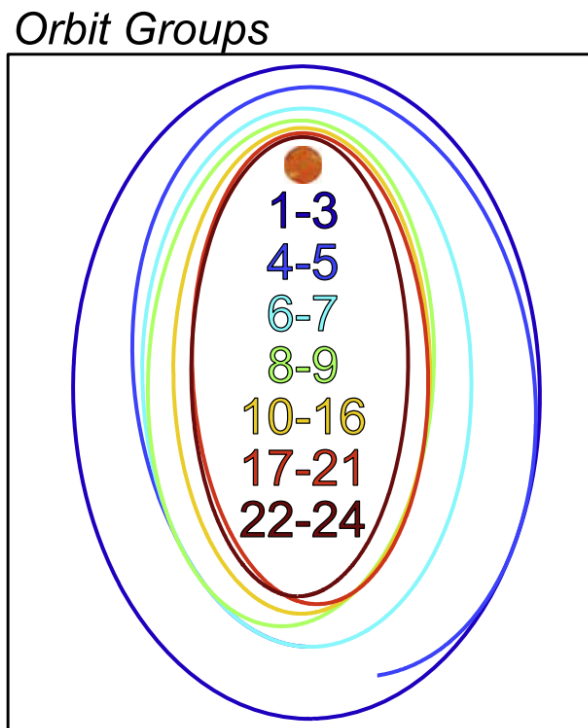
Figure 3.1: All of *Parker Solar Probe*'s planned orbits. Each color represents an orbital group (similar radial distance encounter for each orbit in a said group). (Szalay et al., 2020)

The mission objectives of PSP are: (i) Understanding solar corona/solar wind heating and

acceleration through energy flow, (ii) Exploring energetic particle mechanics, (iii) Construct the structure and dynamics of source solar wind plasma and magnetic fields (Fox et al., 2016).

PSP has four main instruments that are used in achieving the aforementioned objectives. The Solar Wind Electrons Alphas and Protons (SWEAP) is comprised of a Faraday Cup and Solar Probe Analyzers (SPAN), which are focused on measuring the solar wind thermal plasma (ionized hydrogen, helium, and electrons) (Kasper et al., 2016). The Integrated Science Investigation (IS$\odot$IS) is a pair of instruments that focus on measuring higher energy particles, specifically ions and their composition (McComas et al., 2016). The Wide Field Imager for Parker Solar Probe (WISPR) and FIELDS (which does not have a name acronym), are further discussed in this chapter.

This chapter describes the two main instruments used in this study: WISPR and FIELDS, along with the initial modeling of the zodiacal cloud in the inner heliosphere from WISPR.
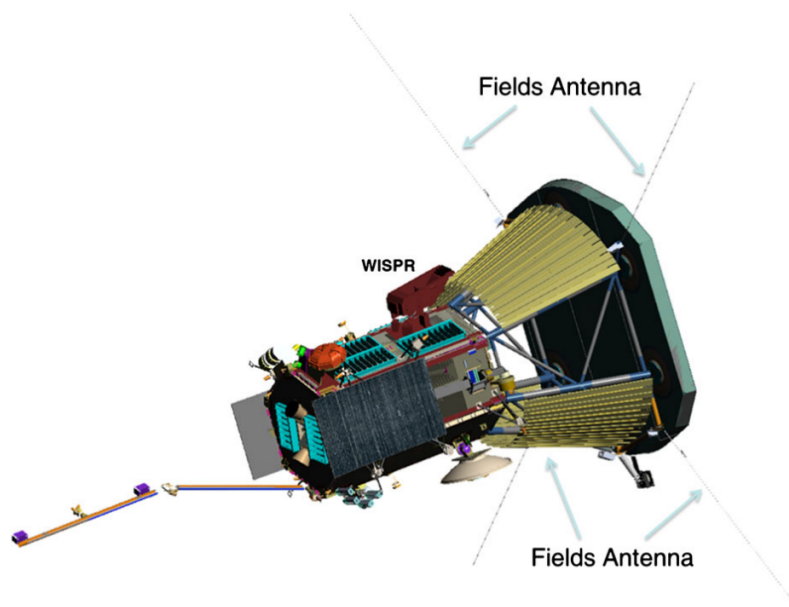
Figure 3.2: WISPR placement on PSP. (Vourlidas et al., 2016)

3.1   Wide Field Imager for Parker Solar Probe(WISPR)

WISPR has two goals that contribute to PSP's mission: (i) Produce data that can be compared to in situ measurements, (ii) Study interplanetary dust and solar wind through imaging of visible sunlight scattered by electrons in the solar wind (Vourlidas et al., 2016). This study incorporates both goals.
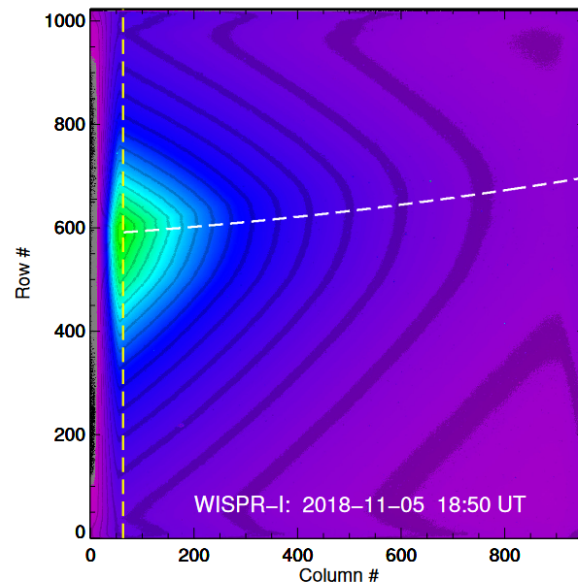
Fig. 1. WISPR-I calibrated image taken during the nominal science encounter in orbit 1. The image is displayed in false colors, with iso-contours in a darker color tone, to illustrate the shape of the F-corona and the location of its symmetry axis (dashed white line across the noses of the iso-contours). For details, see the text.

Figure 3.3: WISPR image with the original description attached. (Stenborg et al., 2021)

WISPR contains two specific modules: an Instrument Data Processing Unit (IDPU) and an instrument model (WIM). Both contain the necessary tools for WISPR to measure and produce images of the inner heliosphere region. WISPR measures photons in the wavelength range of 475 to 740 nm. These photons are produced by Thomson scattered light from electron density fluctuations in the solar wind and from dust particles (Vourlidas et al., 2016).

WISPR allowed the *US Naval Research Laboratory* group to begin the search for the proposed Dust Free Zone (DFZ), and to furthermore explain the characteristics of dust depletion in this region

(see Stenborg et al. (2021) and references therein).
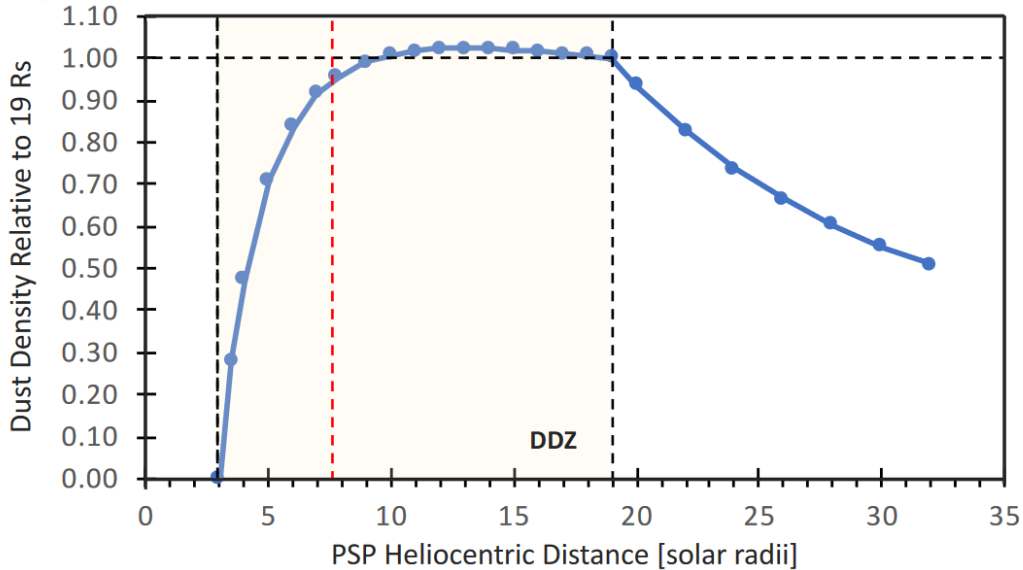
Figure 3.4: WISPR dust density modeled. The red dashed, the vertical line represents the closest distance WISPR was able to image. (Stenborg et al., 2021)

The WISPR group analyzed the change of the F-corona (Electromagnetic radiation produced by sunlight bouncing off dust particles, and identified through Fraunhofer absorption lines) brightness profile radially, using images from the instrument. Their initial observations were that around $19R_\odot$ the dust density begins to lessen. This reduction in dust density is the start of a Dust Depletion Zone (DDZ), which the WISPR team modeled in figure 3.4. The WISPR model shows that the DDZ extends from $19R_\odot$ sunward, stopping at $3R_\odot$. This point marks the start of the DFZ based on their model (Stenborg et al., 2021).

PSP has more than just one method of collecting data on dust. In addition to WISPR's remote sensing imaging techniques, FIELDS may be used to detect dust in situ (see §4).

3.2 FIELDS Instrument

FIELDS measures electric and magnetic fields from DC to 20 MHz using 5 voltage sensors, 2 fluxgate magnetometers, and a search coil magnetometer (SCM) (Bale et al., 2016). Their

placement on the spacecraft is shown in figure 3.5. FIELDS produces a variety of data products. The specific data products used for this study are described in §5.
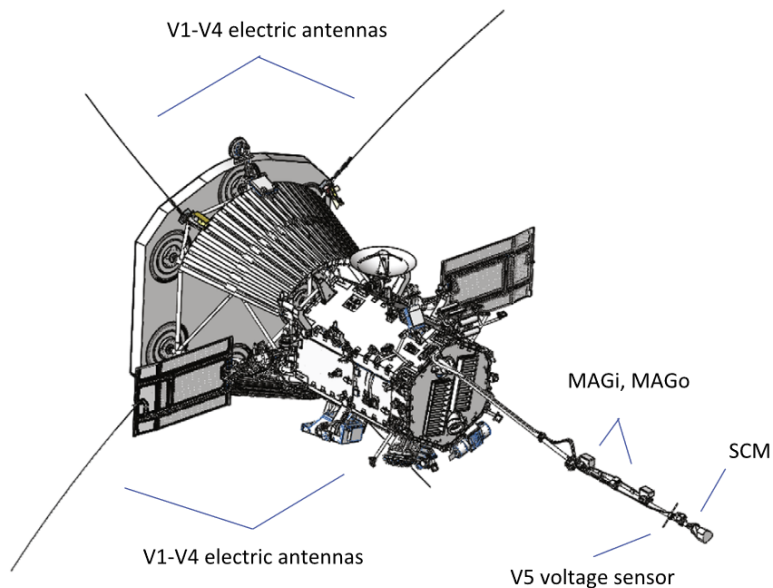
Figure 3.5: FIELDS on PSP. The SCM, two fluxgate magnetometers, and a fifth voltage sensor placed on the tail of the spacecraft. Voltage sensors 1-4 are placed on the body of the spacecraft. (Bale et al., 2016)

FIELDS is effective in measuring dust impacts in situ, even without a dedicated dust detector. This allows scientists to use multiple instruments on PSP to study the same physical process. In this study, FIELDS in-situ dust data are used to build a model of the inner heliosphere's dust characteristics that can be compared with the WISPR DDZ model.

Chapter 4

Interplanetary Dust Impacts

PSP is not the only spacecraft to experience dust impacts in space. However, it is one of the few spacecrafts that has been pelted by dust in inner heliosphere. While instruments dedicated to the characterization of dust particles do exists, dust detection is also possible through the byproducts of a particle-spacecraft impact (Zaslavsky et al., 2012). Previous missions that have used this method of dust detection are: Voyager, Vega, Deep Space 1, Cassini, STEREO, MAVEN, MMS, and Wind (see Gurnett et al. (1983);Laakso et al. (1989);Tsurutani et al. (2004);Kurth et al. (2006);Meyer-Vernet et al. (2009);Andersson et al. (2015);Vaverka et al. (2018);Malaspina et al. (2014)).

This chapter provides a history of dust impact measurements, and addresses the process for PSP.

4.1 Dust Impacts on Previous Mission

Dust particles travel at hypervelocity speeds ($v > 1$ km/s) through space. Spacecraft travel at these speeds as well. When a dust particle collides with a spacecraft, the byproduct is a transient plasma cloud. This plasma cloud can be measured by voltage sensors on the spacecraft as a potential difference between the sensor and spacecraft body (Malaspina et al., 2014).

Voyager 1's detection of dust near Saturn was conducted using 2 voltage antennas, configured as an electric dipole. Voyager 1 produced wideband waveforms over a 50 Hz to 14 kHz frequency range (see 4.2). Sudden changes in the voltage reading indicate an event. The Voyager 1 team were
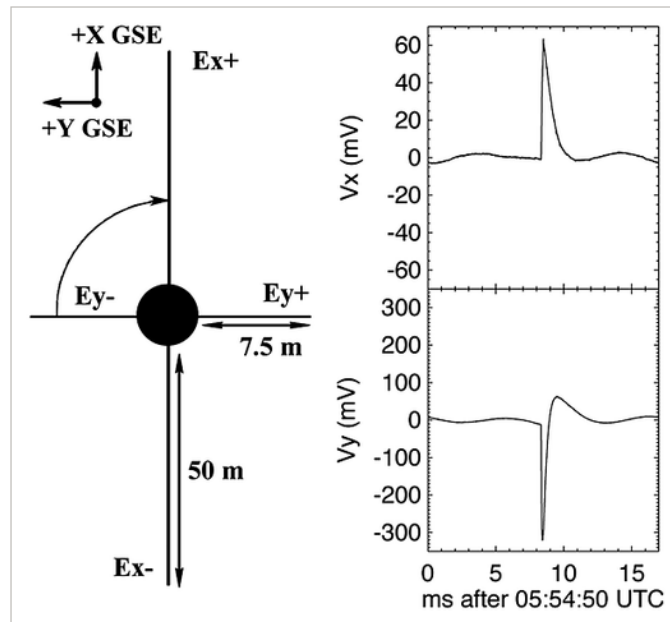
Figure 4.1: *Left:* Geometry of WIND antennas. *Right:* Measured differential potential by the E_x-E_y dipole on 25 December 2007. Measured data was taken during 17 ms TDS waveform capture. (Malaspina et al., 2014)

not able to declare the source of these perturbations as dust impacts. This was later resolved with data from Voyager 2. In addition to getting closer to Saturn than Voyager 1, Voyager 2 also collected sound recordings. The sound recordings indicated that Voyager 2 was being pelted by particles in space on its travel through Saturn's rings. The Voyager 2 team was able to then confirm dust in that region using this method (for more info see (Gurnett et al., 1983) and references therein).

The Solar Terrestrial Relations Observatory (STEREO) was another mission where the detection of wave bursts occurred. Originally the STEREO team was not sure whether the changes in the wave burst were caused by dust impacts, citing (Gurnett et al., 1983). The main cause of concern here was that, while both Voyagers experienced dust impacts, STEREO conduced research closer to the sun than both Voyagers. Their method of measurement was also to take the electrical signal of dust impacts in a dipole configuration, but the geometrical configuration of the spacecraft made the data harder to analyze compared to Voyager. The STEREO group's modeling of dust in a region closer to the sun than Voyager yielded results that indicated dust impacts (Meyer-Vernet
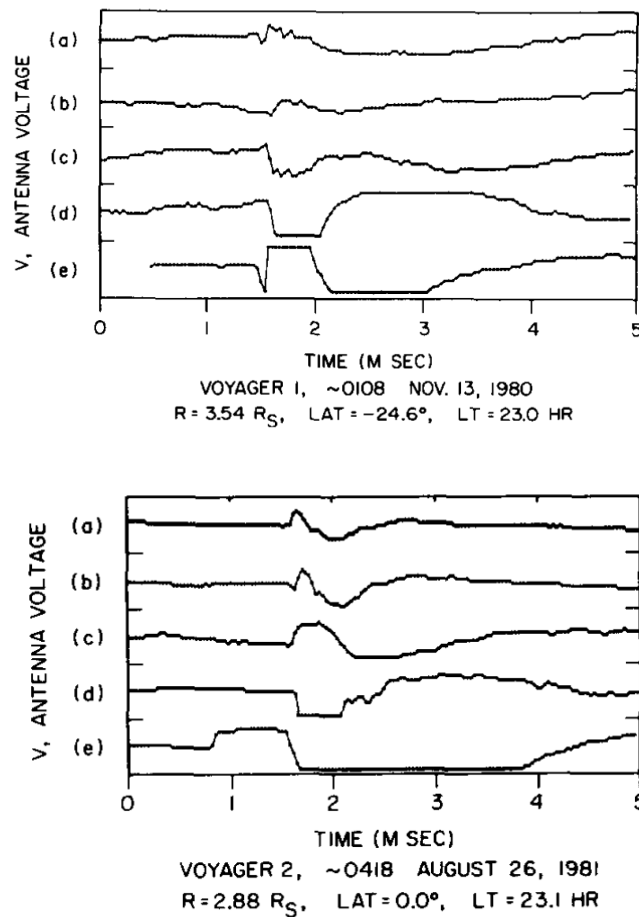
Figure 4.2: *Top:* Wideband waveform representing particle impacts on Voyager 1. Small impact rate of four impacts per second *Bottom:* Wideband waveform representing particle impacts on Voyager 2. Impact rate of several hundred impacts per second. (Gurnett et al., 1983)

et al., 2009).

PSP's FIELDS instrument can be used to explore interplanetary dust even closer to the sun using this method. PSP's four voltage antennas located on the main body of the spacecraft 3.5, are able to measure the voltage potential due to dust impact plasma clouds(see §5).

This study uses FIELDS dust impact detection along with the remote sensing observations by WISPR to test the theory of the inner heliosphere DFZ. Learning about dust in this region allows for a deeper understanding of how stars interact with dust in other stellar environments and further understanding of the dust destruction process.
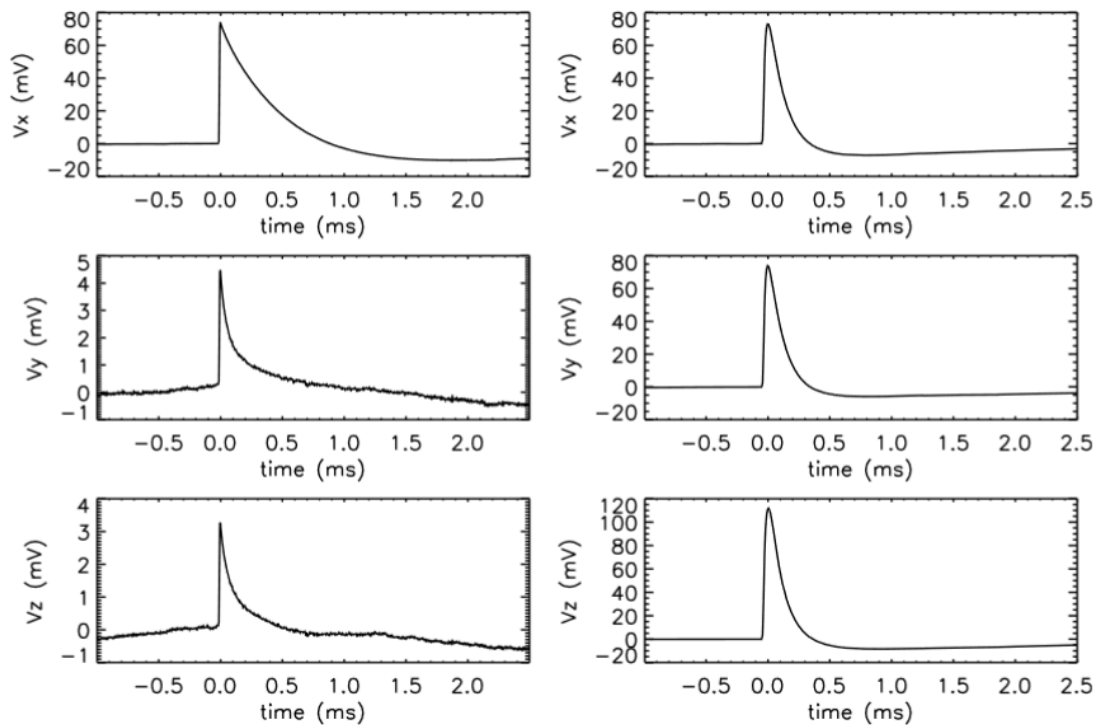
Figure 3. Typical examples of voltage impulses observed by the TDS onboard STEREO A. (top to bottom) The voltage observed on the X, Y and Z monopoles. The timescale is shifted so that the time is 0 when the signal reaches its maximum on the X monopole. (left) An example of a single hit (1 January, 2009, 2:54 UT). (right) An example of a triple hit (31 March, 2007, 14:48 UT) (see section 2.3 for the definition of the single and triple hits, and sections 2.4.2 and 2.4.3 for their physical interpretation).

Figure 4.3: Potentials measured by STEREO, with original description attached. (Zaslavsky et al., 2012)

Chapter 5

Data

PSP has the direct ability to measure dust through the resultant plasma cloud caused by collisions. This data collection method proves useful in producing data, able to describe dust rates in the inner heliosphere.

This chapter will discuss in detail the data products used for this study, in addition to the methods of error correction applied to the acquired data.

5.1   FIELDS Data Products and Burst Measurement

FIELDS has 3 receivers of electric field data: (i) Digital Fields Board (DFB), (ii) Time Domain Sampler(TDS), and (iii) Radio Frequency Spectrometer(RFS). Each receiver produces many different data products (based on the frequency range covered), some of which can be used to study dust in situ.

DFB processes signals from the voltage sensors and the SCM over frequencies from DC to 75 kHz (Bale et al., 2016). SCM signals were not used for this study. The DFB generates many DC-coupled and AC-coupled signals that can be processed into data products (see Table 1 in Malaspina et al. (2016)). The main DFB data product used for this study is burst. Burst data consists of 6 channels containing time series data sampled at $150000/2^n$ samples/s, for $n \in \mathbb{Z}$. Each channel of the burst contains 2^{19} samples. While DFB burst is continuously produced, the signal written to FIELDS' memory comes from the burst with the largest amplitude in 20-minute intervals. After each orbit, a human selects portions of the stored data, which is then transmitted to earth. 0.01%

of total sampled burst data makes it to earth (Malaspina et al., 2016). This study uses burst data signals from DC-coupled single-ended signals (vdc), from AC-coupled single-ended signals (vac), from DC-coupled differential signals (dvdc), and from AC-coupled differential signals (dvac) (see §3).

TDS processes signals from the voltage sensors and the SCM over frequencies from 5 kHz to 1 MHz (Bale et al., 2016). The single data from TDS used was the TDSmax. Over n seconds, where n is either 7s or 60s, TDSmax outputs the peak value of the largest signal observed. A 7s window frame is set for a radial distance less than $55R_\odot$(defined as an orbit encounter), while the 60s is set for a radial distance greater than $55R_\odot$. Additionally, TDSmax outputs the root mean squared (RMS) value associated with the peak. This study uses only the V_2 antenna voltage signal sampled by TDSmax. This is because V_2 is the only signal sampled continuously by TDSmax over the mission duration.

RFS processes signals from the voltage sensors over frequencies from 100 kHz to 20 MHz(Bale et al., 2016). Signals from RFS are primarily used for radio wave studies and therefore are not used in this study.

5.2   Sources of Error

The main issue with a dust study using Parker Solar Probe is that the spacecraft does not have a dedicated dust detector. Instead, we use the voltage antennas to measure a potential difference across the antenna and body. Large spikes of asymmetric shape as shown in figure 5.1 are the indicators of a dust impact. Given that we measure dust using plasma clouds (see §4) it can be hard to distinguish between a plasma wave and a dust impact. We label this as plasma wave error. To resolve wave error, we require that a dust detection has a peak amplitude, as measured by TDSmax, greater than $50mV$, and the peak amplitude to RMS ratio given is greater than 100. This condition selects spiky, impulsive signals (dust) and removes sine-like signals (waves).

Additionally, there are cases where the spacecraft records no data. We call this dead time. To correct for dead time error, we remove samples with NaN values in the TDSmax data product.
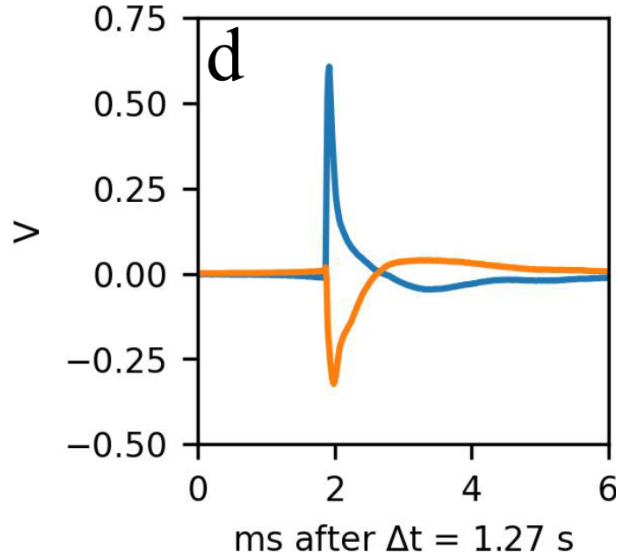
Figure 5.1: Example of voltage signals as a time-series waveform near dust impact. The orange is representative of V_{34} and the blue of V_{12}. (Malaspina et al., 2023)

This slightly changes the dust count rate near perihelion (see fig. 5.9). With both dead time and plasma wave error corrected, there is one more error to consider.

The method TDSmax employs for measuring dust is incapable of measuring multiple impacts in a given 7s time window. This means that if there are any other dust impacts in that window of slightly lower amplitude, they will not be recorded. Therefore, there is a possibility of under-counting the number of dust impacts during an orbit.

To correct this error, two methods of statistical error analysis were applied. First, a probabilistic error correction based on radial distance, and second a waiting time error correction based on the time between impacts.

5.3   Probabilistic Error Correction

The first method of approaching under-counting is to take DFB in situ dust data and compute the probability of having N impacts in a given 3.5s interval for $N \in \{1, 2, 3, 4\}$, where each impact is treated as an independent event. To continue with the analysis, a database of DFB in-situ impacts was built.

5.3.1   Power Spectral Density Spectrograms

DFB burst data were used because they have higher time resolution than TDSmax.
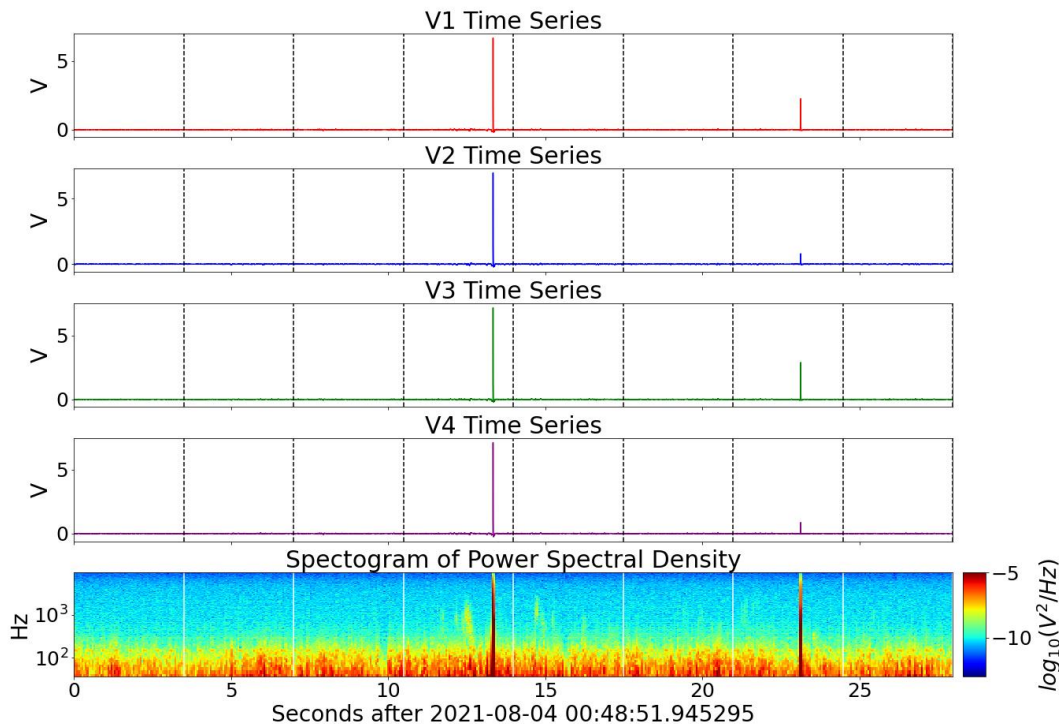
Figure 5.2: Example of a time series burst produced from AC-coupled single-ended signals (vac) during PSP's 9th orbit. From top to bottom: The first two plots are the voltage signal time series, while the bottom graph is the spectrogram detailing the DFB voltage differential data as Power Spectral Density.

The easiest way to identify dust impacts in DFB burst data is to apply a windowed fast Fourier transform (FFT) to produce a spectrogram. The spectrogram can then be plotted along with the DFB voltage data to identify and tabulate dust impacts. Figures 5.2 and 5.3 are examples of how dust impacts were counted.

Note that 5.2 has a longer duration when compared to 5.3. In every encounter, the burst time duration ranged in values of 3.5×2^n seconds for $n \in \{1, 2, 3, ..., 8\}$. The standardization of the database was done by examining 3.5s windows for each burst. This is shown using the dotted
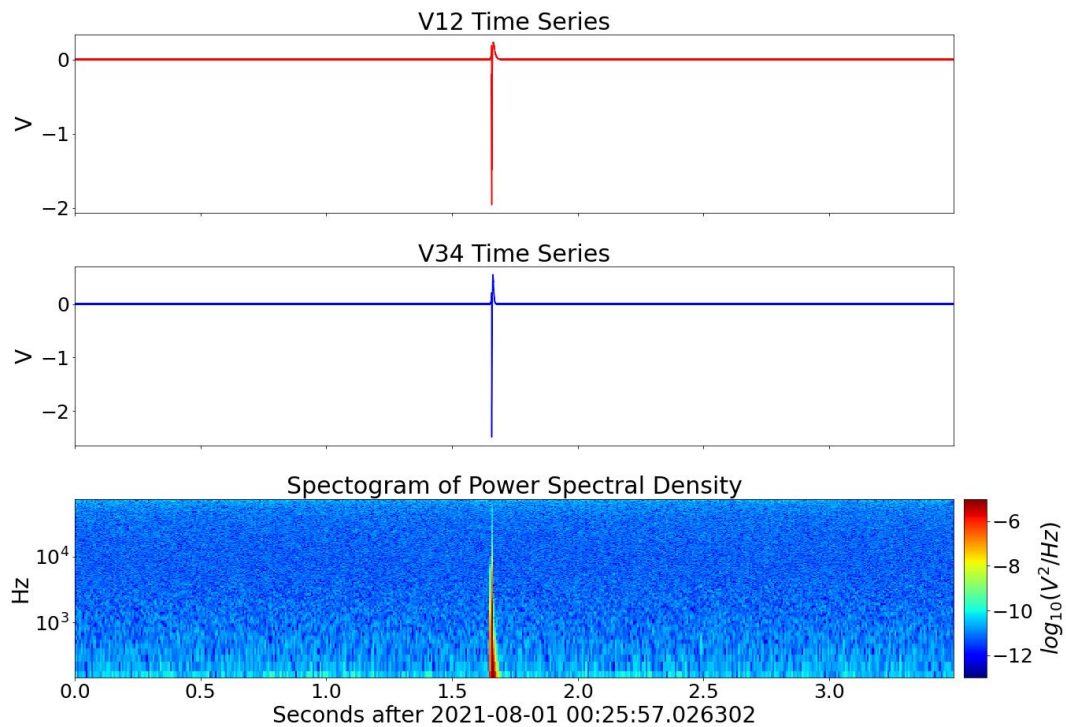
Figure 5.3: Example of a time series burst produced from AC-coupled differential signals (dvac) during PSP's 9th orbit. From top to bottom: The first two plots are the voltage signal time series, while the bottom graph is the spectrogram detailing the DFB voltage differential data as Power Spectral Density.

vertical lines in figure 5.3.

To count a dust impact in both figures 5.2 and 5.3, there are 2 distinct characteristics that a dust impact must have:(i) There is a spike in both voltage time series and spectrogram, that occur simultaneously, (ii) The spectrogram spike is high amplitude (indicated by red or orange color) over most of the frequency range.

This procedure was applied to all DFB burst data from orbits 1 through 10 and allowed us to make the following statistical analysis.

5.3.2 Construction of Probabilistic Error Correction

To understand what type of correction had to be applied, we first needed to see under what conditions the dust impacts behaved like a Poisson random distribution.
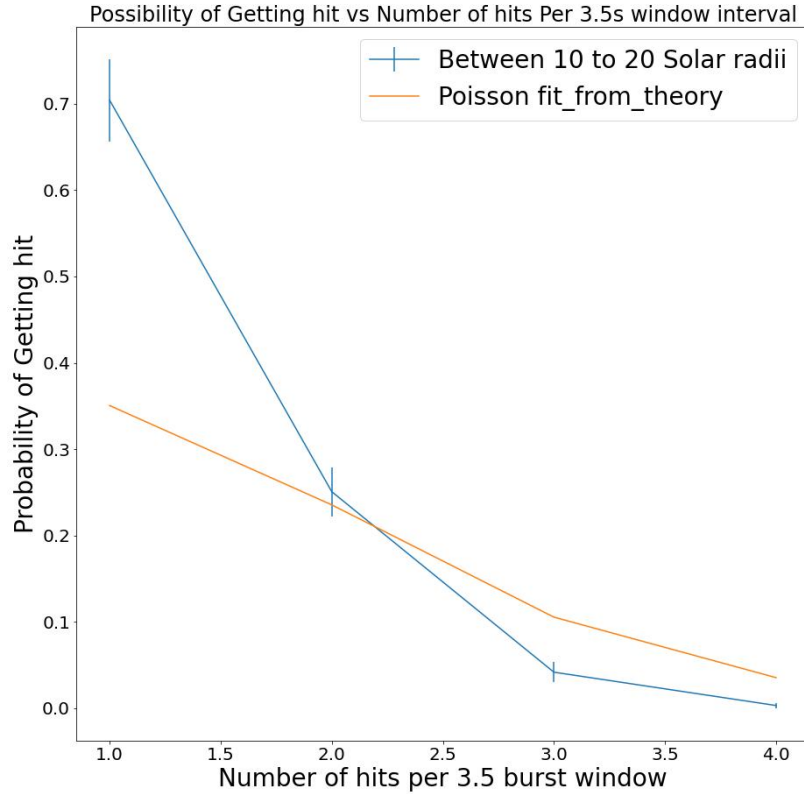
Figure 5.4: The probability of N impacts vs $N = k$ impacts for $k \in \{1, 2, 3, 4\}$ between $10R_{\odot}$ to $20R_{\odot}$ as seen in 3.5s burst window. The curve shown in blue is the organized in-situ data as computed by 5.1. The curve shown in orange is the Poisson probability equation from probability theory as computed by 5.2.

The effect that radial distance has on the impact rate was studied. All dust impacts in the database were organized into radial distance bins of $10R_{\odot}$, ranging from $10R_{\odot}$ to $60R_{\odot}$ and beyond. Once the organization of data points was done, the total number of impacts in that distance bin was calculated and the probabilities of the impacts were computed as:

$$\mathbb{P}(\text{N impacts}) = \frac{\text{number of intervals with N impacts}}{\text{total number of impacts in distance bin}} \tag{5.1}$$
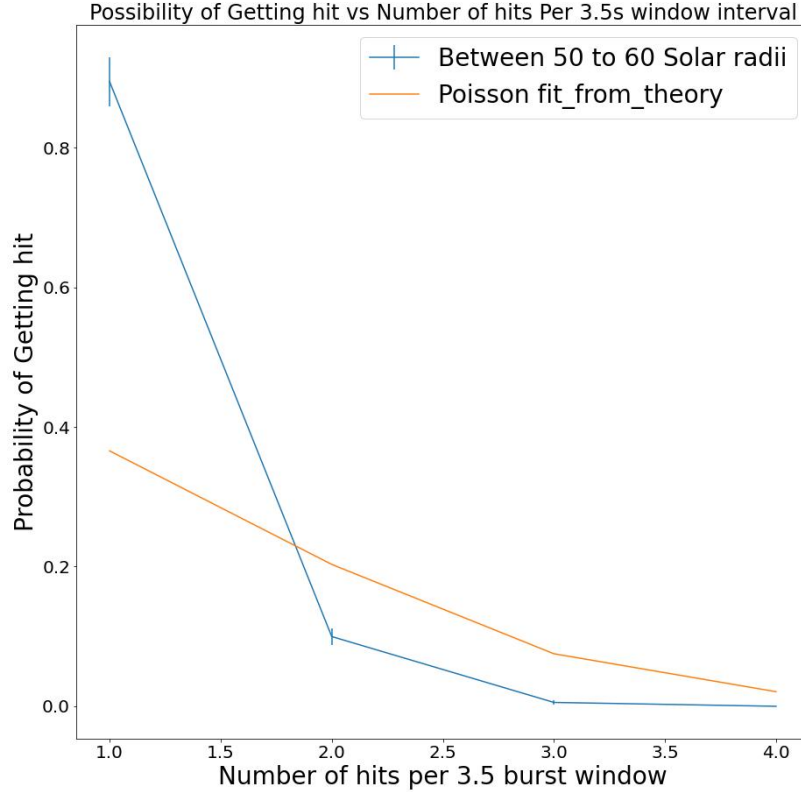
Figure 5.5: The probability of N impacts vs $N = k$ impacts for $k \in \{1, 2, 3, 4\}$ between $50R_\odot$ to $60R_\odot$ as seen in 3.5s burst window. The curve shown in blue is the organized in-situ data as computed by 5.1. The curve shown in orange is the Poisson probability equation from probability theory as computed by 5.2.

Observations show that there is a radial dependence of the probability distribution. Figures 5.4 and 5.5 were chosen to show the closest and farthest distance bins to the sun. As we radially approach the sun inwards, the probability of $N > 1$ impacts grows. Fig 5.4 has an approximate probability of 26% for $N = 2$ impacts, while for figure 5.5 that probability lowers to 10%.

Additionally, figures 5.4 and 5.5 have the theoretical Poisson curve fitted from the following equation:

$$\mathbb{P}(X = x) = \frac{\mu^x e^{-\mu}}{x!} \tag{5.2}$$

where μ is the mean number of impacts that occur in the bin.

The theory curve is below the in situ probability distribution and did not fit for any value of μ. Therefore, we conclude these distributions are not Poisson-like. Thus, an empirical correction was applied.

The probability of more than one impact occurring within each TDSmax observation window was determined by randomly drawing from a distribution defined by the measured probabilities of finding a given value of N. A different probability distribution was applied to the TDSmax data within each radial distance bin.

This method has a caveat. The analysis uses 3.5s window sizes. TDSmax operates on 7s and greater window sizes. This method of error correction may not apply to time intervals greater than 3.5s. Therefore, it is important to see if another method would yield a different result.

5.4 Waiting Time Error Correction

The second method of under-count correction is to observe the time between impacts. The waiting time error analysis is done directly from TDSmax's data of Encounters 10 through 13. We denote μ_{wc} as the impact rate of the dust. This is produced from the interpolation of the 8 hr impact rate, acquired from TDSmax, to each dust impact's time as defined.

The events are separated by 20 bins of width $\triangle\mu_{wc} = 0.25$ in units of impacts/min. The minimum value for μ_{wc} is 0 impacts/min and the maximum is for μ_{wc} is 5 impacts/min. Each bin allows for the calculation of the waiting time between impacts, which is then modeled by a histogram. The histogram ranged from 0 s to 50×6.99 s (the shortest time window for TDSmax data collection) (Malaspina et al., 2023).

Given that we assume the dust impacts are randomly distributed unlike our probability analysis, we can formulate a distribution of the waiting time between impacts as the following
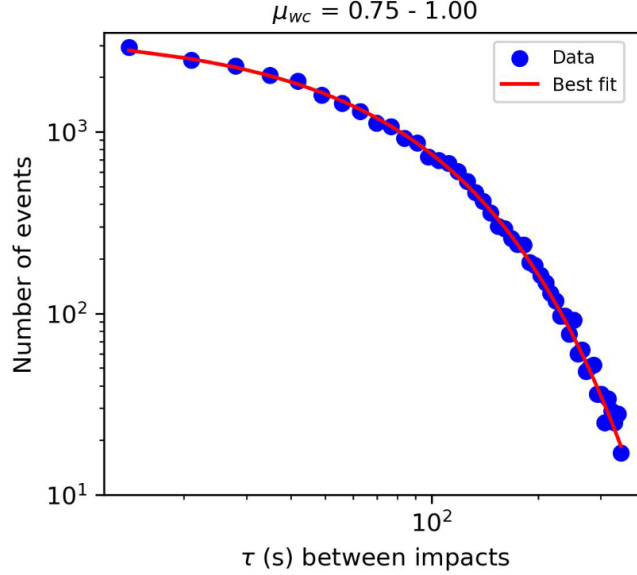
Figure 5.6: Waiting time distribution of dust impacts from Orbits 1 through 13. The 8-hr impact rate is between 0.75 impacts/min and 1.00 impacts/min. The thin red line is a best-fit curve that comes from equation 5.3 with $\mu_{corr} = 0.91$. (Malaspina et al., 2023)

equation:

$$f(\tau) = A(\mu_{corr}\tau)e^{-\mu_{corr}\tau} \tag{5.3}$$

where A is a normalization constant, τ is the time between impacts, and μ_{corr} is impact rate corrected for under-counting (impacts/s) (Malaspina et al., 2023).

For each bin, the distribution is fit using equation 5.3 along with a nonlinear least squares method, setting μ_{corr} and A to be fit parameters. Initial guesses for the fit can be done by setting μ_{corr} using μ_{wc} values.

An example of this fitting is shown in figure 5.6, where we have taken the $\mu_{wc} = 0.75$ impacts/min to μ_{wc} impacts/min bin. The red line indicates the best-fit curve, given $\mu_{corr} = 0.91$ impacts/min.

After analyzing each bin, figure 5.7 was produced to show the percentage of under-counting we experience for each N amount of impacts and to establish a method of correction. The blue linear line represents no corrections made to the dust and serves as a reference point for the corrected
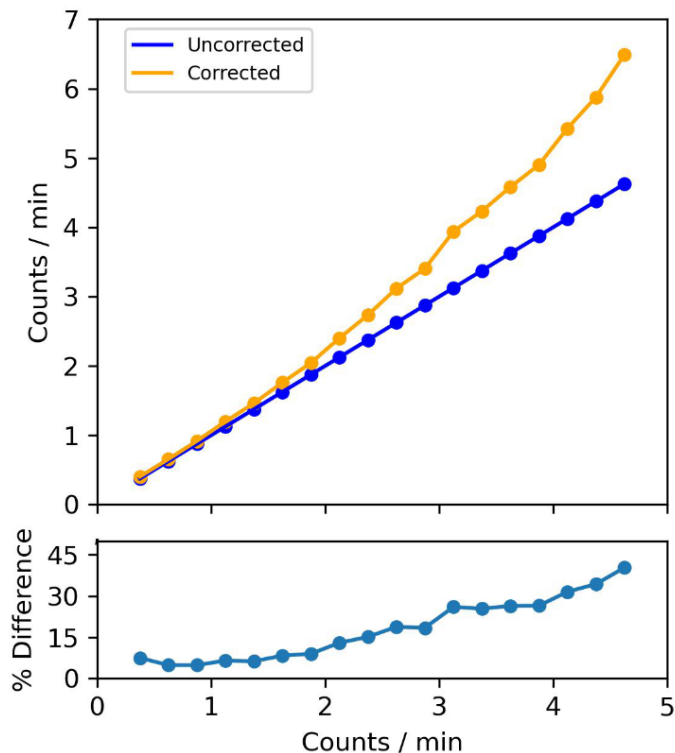
Figure 5.7: *Top:* Under-counting corrected impact rates shown by the orange curve, as a function of non-corrected impact rates. A blue linear line that represents no correction is shown for comparison. *Bottom:* The difference between the uncorrected and under-counting corrected impact rates as a function of non-corrected impact rates shown as a percentage. (Malaspina et al., 2023)

line. The orange line suggests that the correction is small for $N = 1$ and $N = 2$ impacts, and large for $N = 3$ and $N = 4$.

Given this correction, we now will compare the two methods and discuss which method was chosen for the rest of the study.

5.5   Comparison of Probabilistic and Waiting Time Corrections

Figures 5.8 and 5.9 both show the correction methods applied to in situ dust count rate. Both methods exhibit the same qualities, with the under-counting being strongest near perihelion and weakest as PSP leaves the sun. While both of the methods have shown to be effective in fixing the under-count correction, the waiting time method is the method that is used for the remainder of this analysis.
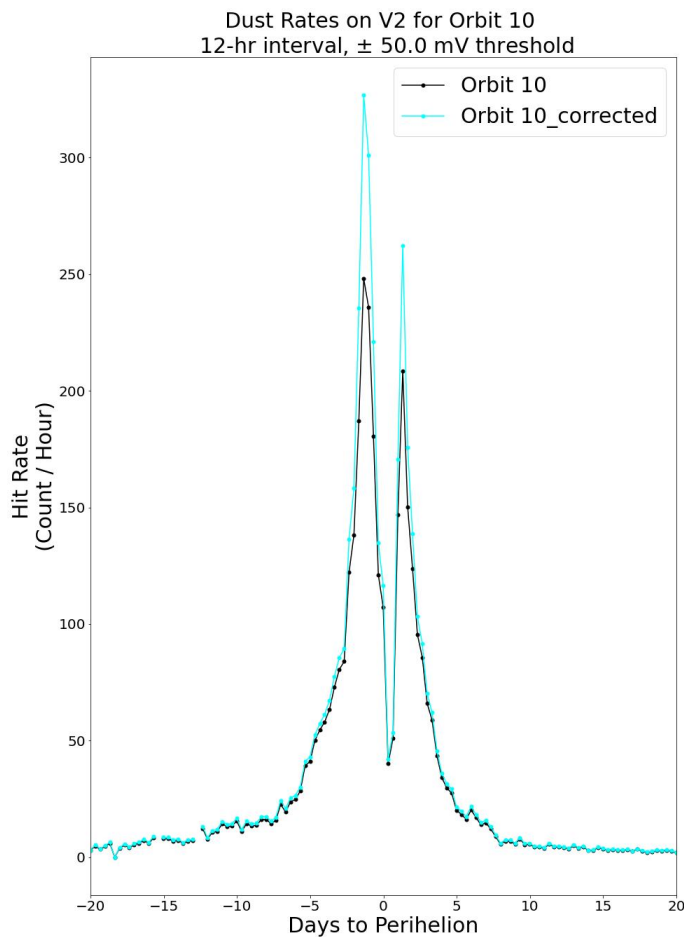
Figure 5.8: Orbit 10 count rate vs the days before (negative) and after (positive) perihelion. The cyan line is the under-count corrected rate from the probability method. The black line is the original dust rate with plasma wave and dead time correction.

Firstly, the waiting time method uses window sizes of 7s or greater, while the probability method uses 3.5s window sizes. As discussed above, the waiting time method is directly applicable to the timescales of the TDSmax data. This is because the waiting time method uses 7s as its smallest window size for the analysis. Trying to use the probability method for timescales larger than 3.5s yielded a non-Poisson distribution. The waiting time method yielded a Poisson distribution. The reason for this disagreement has not been resolved yet.
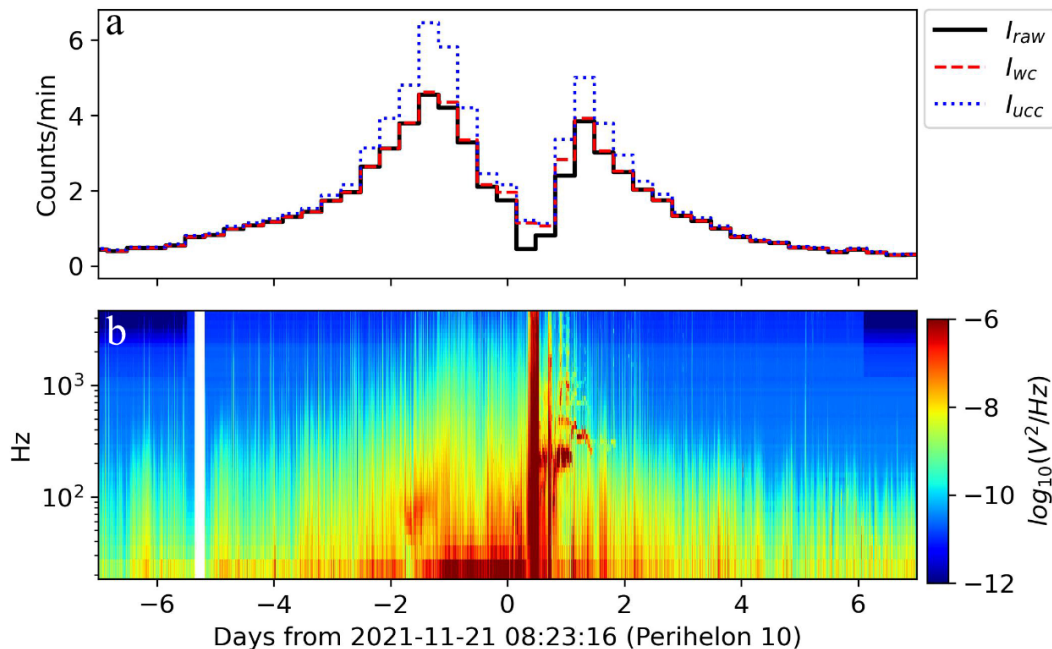
Figure 5.9: *Top:* Dust impact rate for Encounter 10 modeled with the: non-corrected rate(I_{raw}, solid black line), the rate including plasma wave and dead time corrections(I_{wc}, red dashed line), and the rate with the under-count correction and previously mentioned corrections(I_{ucc}, dotted blue line. *Bottom:* Spectrogram for differential voltage power spectral density as a function of time, detailing the activity of plasma waves during Encounter 10. (Malaspina et al., 2023)

Secondly, both TDSmax and DFB data have different frequency bandpasses. The TDSmax uses a middle frequency while the DFB data is at a low frequency. Therefore, it is not clear that DFB and TDSmax detect the same set of dust impacts.

Waiting time is overall more self-consistent and the method that was used for the rest of this study.

Chapter 6

Model

This study involves a data-model comparison between a derived Inner Heliosphere Dust Model and PSP's in-situ measurements. To derive the Inner Heliosphere Dust Model, we start with the *U.S. Naval Research Laboratory* WISPR group's model of dust density relative to $19R_\odot$ (Stenborg et al., 2021). This model only considers dust particles large enough to scatter visible light(α meteoroids). The WISPR model was used to construct models for both α and β meteorites. These models were then scaled to 1 AU and combined to form the Inner Heliosphere Dust Model (6.1). The details of this combination are described in the following sections.
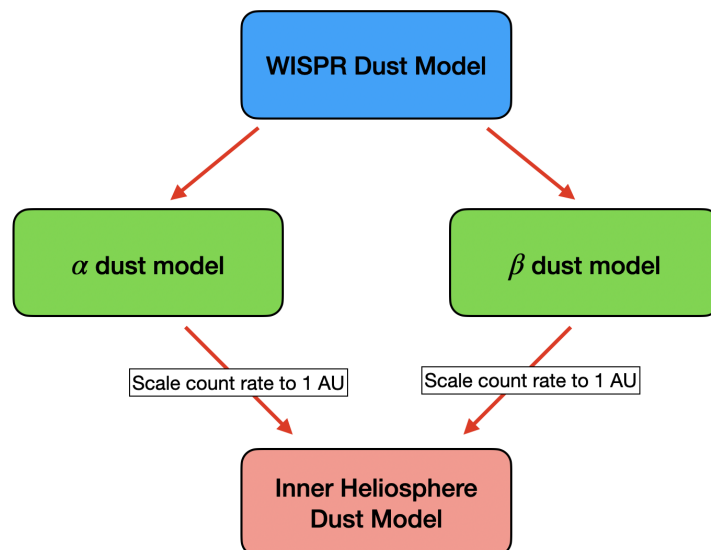
Figure 6.1: Graphical representation of Inner Heliosphere Dust Model construction

6.1   WISPR Dust Density Converted Into Count Rate

The WISPR model does not have the same units as in-situ dust, therefore to compare this model to our in-situ data, we had to describe the WISPR data using the following equation:

$$R_c = \rho_\alpha A v_\alpha + \rho_\beta A v_\beta \tag{6.1}$$

where ρ_α and ρ_β are density functions for α and β respectively, A is the cross-sectional area of impact detection on the spacecraft. v_α and v_β are the velocity of α and β meteorites. The cross-sectional area of the spacecraft(A) is assumed to be identical for α and β meteorites held constant over the orbit, therefore we assume $A = 2m^2$. Now the dust velocity and density need to be determined.
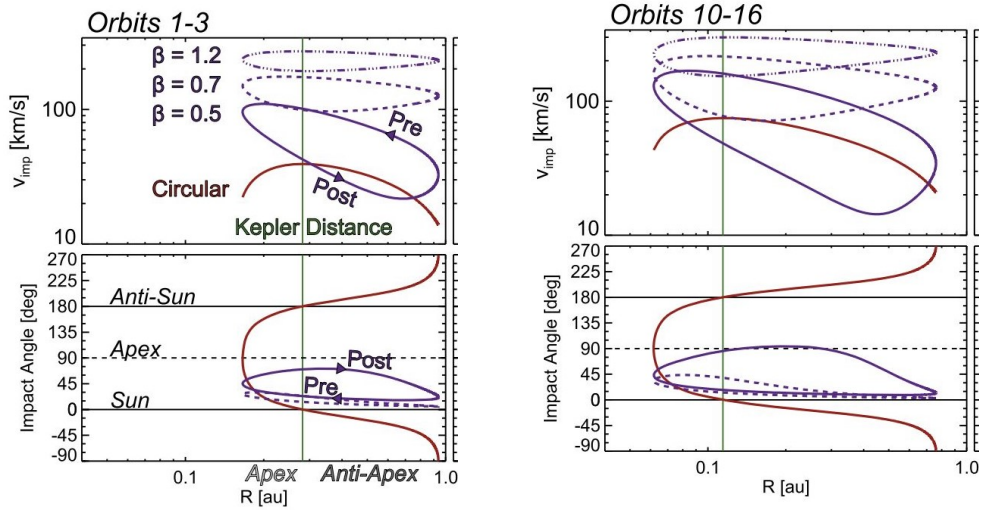
Figure 6.2: *Left:* Velocity of dust relative to PSP at different radial distances for orbits 1 through 3 for both α(red) and β(purple) meteorites *Right:* Velocity of dust relative to PSP at different radial distances for orbits 10 through 16 for both α(red) and β(purple) meteorites. There are two additional plots regarding impact angles of dust, but they were not used in this study. (Szalay et al., 2020)

A prior study defined α and β meteorite velocities in the inner heliosphere (Szalay et al., 2020). Figure 6.2 shows velocities derived for several values of β. The β meteorite velocities have a pre-perihelion and post-perihelion component, therefore equation 6.1 needs to be evaluated for

pre-perihelion and post-perihelion separately. In addition, we convert all velocity values to m/hr.

The Inner Heliosphere Dust Model will be compared to in-situ data from encounters 10 through 13(closest approach to the Sun of 13.2R$_\odot$). Therefore, we use velocity curves from 6.2 relevant to those encounters. There are three β values plotted. As such, β meteoroid models were created for each in part.

The density functions are constructed from figure 3.4. The model was split into the following piecewise functions as follows:

$$\rho_\alpha = \begin{cases} 0 & r \leq 3 \\ 0.906 ln(r) - 0.8188 & 3 \leq r \leq 9 \\ 1 & 9 \leq r \leq 19 \\ \left(\frac{19}{r}\right)^{1.3} & 19 \leq r \end{cases} \tag{6.2}$$

$$\rho_\beta = \begin{cases} 0 & r \leq 3 \\ 0.906 ln(r) - 0.8188 & 3 \leq r \leq 9 \\ 1 & 9 \leq r \leq 19 \\ \left(\frac{19}{r}\right)^{2} & 19 \leq r \end{cases} \tag{6.3}$$

The WISPR model is split into three regions. The innermost region is the proposed dust-free zone. The next region is the proposed dust-depletion zone. Dust density is assumed to be flat in the third region. The last section of each piecewise equation is constructed using knowledge of how α and β meteoroid densities fall off with radial distance from the sun.

We assume that the shape of the β meteoroid piece-wise function is identical to that of the α meteoroid piece-wise function in the range of $0 \leq r \leq 19$ because β meteoroids are produced by collisional breakup of α meteoroids in this region (see Szalay et al. (2020) and references therein).

The description of the dust density is still incomplete. Equations 6.2 and 6.3 are still dimensionless. We therefore scale the equations such that the α and β meteorite models match

observations of α and β meteorite fluxes at 1AU (215R$_\odot$). The final units are $counts/m^3$. We compute the dust density of α and β meteorites using their respective fluxes and estimated velocities to get (see Cooke et al. (1993),Grün et al. (1983) and references therein):

$$\rho_\alpha(215R_\odot) = \frac{\alpha_{flux}}{\alpha_{vel}} = \frac{1\text{x}10^{-6}\,\frac{counts}{m^2 s}}{18\text{x}10^3\,\frac{m}{s}} = 5.5\text{x}10^{-11}\frac{counts}{m^3} \tag{6.4}$$

$$\rho_\beta(215R_\odot) = \frac{\beta_{flux}}{\beta_{vel}} = \frac{1\text{x}10^{-15}\,\frac{counts}{m^2 s}}{50\text{x}10^3\,\frac{m}{s}} = 2\text{x}10^{-9}\frac{counts}{m^3} \tag{6.5}$$

We then construct the WISPR dust density at 215R$_\odot$ using the following set of equations:

$$\rho_{\alpha\text{WISPR}}(r) = \rho_\alpha(r=19)\left(\frac{R_0}{r}\right)^{1.3} \quad \rho_{\beta\text{WISPR}}(r) = \rho_\beta(r=19)\left(\frac{R_0}{r}\right)^{2} \tag{6.6}$$

where $R_0 = 19R_\odot$ in both equations.

The assumption of identical model shape simplifies equation 6.6 with the condition that $\rho_\alpha(r=19) = \rho_\beta(r=19) = 1$. Thus the equations become:

$$\rho_{\alpha\text{WISPR}}(r) = \left(\frac{19}{r}\right)^{1.3} \quad \rho_{\beta\text{WISPR}}(r) = \left(\frac{19}{r}\right)^{2} \tag{6.7}$$

Equation 6.7 at $1AU = 215$R$_\odot$ results in:

$$\rho_{\alpha\text{WISPR}}(r=215\text{R}_\odot) = \left(\frac{19}{215}\right)^{1.3} = 4.27\text{x}10^{-2} \quad \rho_{\beta\text{WISPR}}(r=215\text{R}_\odot) = \left(\frac{19}{215}\right)^{2} = 7.81\text{x}10^{-3} \tag{6.8}$$

Using the results from: 6.8, 6.4 and 6.5, the following ratios are constructed:

$$\frac{\rho_\alpha(r=215\text{R}_\odot)}{\rho_{\alpha\text{WISPR}}(r=215\text{R}_\odot)} = \frac{\rho_{\alpha\text{WISPR}}(r=19\text{R}_\odot)}{\rho_{\alpha\text{WISPR}}(r=19\text{R}_\odot)} \quad \frac{\rho_\beta(r=215\text{R}_\odot)}{\rho_{\beta\text{WISPR}}(r=215\text{R}_\odot)} = \frac{\rho_\beta(r=19\text{R}_\odot)}{\rho_{\beta\text{WISPR}}(r=19\text{R}_\odot)} \tag{6.9}$$

Having solved for all terms except $\rho_\alpha(r=19\text{R}_\odot)$, the set of ratios may be rearranged as:

$$\rho_\alpha(r=19\text{R}_\odot) = \frac{\rho_\alpha(r=215\text{R}_\odot)\rho_{\alpha\text{WISPR}}(r=19\text{R}_\odot)}{\rho_{\alpha\text{WISPR}}(r=215\text{R}_\odot)} \tag{6.10}$$

$$\rho_\beta(r = 19\text{R}_\odot) = \frac{\rho_\beta(r = 215\text{R}_\odot)\rho_{\beta\text{WISPR}}(r = 19\text{R}_\odot)}{\rho_{\beta\text{WISPR}}(r = 215\text{R}_\odot)} \tag{6.11}$$

Including numerical values for each variable, the resulting scale factors are:

$$\rho_\alpha(r = 19\text{R}_\odot) = \frac{5.55 \times 10^{-11}}{4.27 \times 10^{-2}} = 1.29\text{x}10^{-9}\frac{counts}{m^3} \tag{6.12}$$

$$\rho_\beta(r = 19\text{R}_\odot) = \frac{4.27\text{x}10^{-9}}{7.8\text{x}10^{-3}} = 2.56\text{x}10^{-7}\frac{counts}{m^3} \tag{6.13}$$

Therefore, equation 6.1 is re-calibrated with these dimensional scaling factors, and given our assumption of A we can state that our rate of impact equation is:

$$R_c = (1.29\text{x}10^{-9}\rho_\alpha)2v_\alpha + (2.56\text{x}10^{-7}\rho_\beta)2v_\beta \tag{6.14}$$

Equation 6.14 describes the full Inner Heliosphere Dust Model. We can now compare this with the in situ data.

6.2 Data Model Comparison Between the Inner Heliosphere Dust Model and In Situ Data

First, we examine how α and β separately influence the total dust rate from the Inner Heliosphere Dust Model. Figures 6.3 shows the predicted α and β dust count rates for three different β values: 0.5β, 0.7β, and 1.2β. We conclude that the α dust population has minimal effect on the total dust count rate.

We now move on to directly comparing the Inner Heliosphere Dust Model with in situ measurements. Because encounters 10 through 16 all have the same orbital geometry, we plot the average in-situ dust rate from Encounters 10 through 13.

To test the validity of the WISPR team's conclusion that a DDZ exists, we compared the in-situ dust data with two iterations of the Inner Heliosphere Dust Model: one with a DDZ and one without a DDZ.

Figure 6.4 shows the Inner Heliosphere Dust Model prediction with and without a DDZ, for each β value. An initial observation can be made for the 1.2β case. The Inner Heliosphere Dust

Model prediction is too high compared to in situ data, for both DDZ and non-DDZ cases. Figure 6.4 for 1.2β has peaks at a value larger than the in-situ data, such that we may directly state that 1.2β meteorites negligibly contribute to in-situ measurements.

We conclude that 0.5β and 0.7β are likely to be the dominant observable for in situ measurements. Both 6.4 for 0.5β and 6.4 for 0.7β have the DDZ dust rate curve following the overall trend of the in situ data. The peak for 0.7β is larger than the in situ data but exhibits the same characteristics. The non-DDZ dust rate curve has a peak, which is a large spike. In addition, that peak is closer to the sun, at around $9\mathrm{R}_\odot$, rather than the in-situ $19\mathrm{R}_\odot$ peak.

Since the in situ data closely follow the Inner Heliosphere Dust Model (with DDZ) curve, we can state that at $19\mathrm{R}_\odot$ we are beginning to see decreasing dust density. This confirms the existence of the DDZ. However, there are limitations to the study that should be considered.
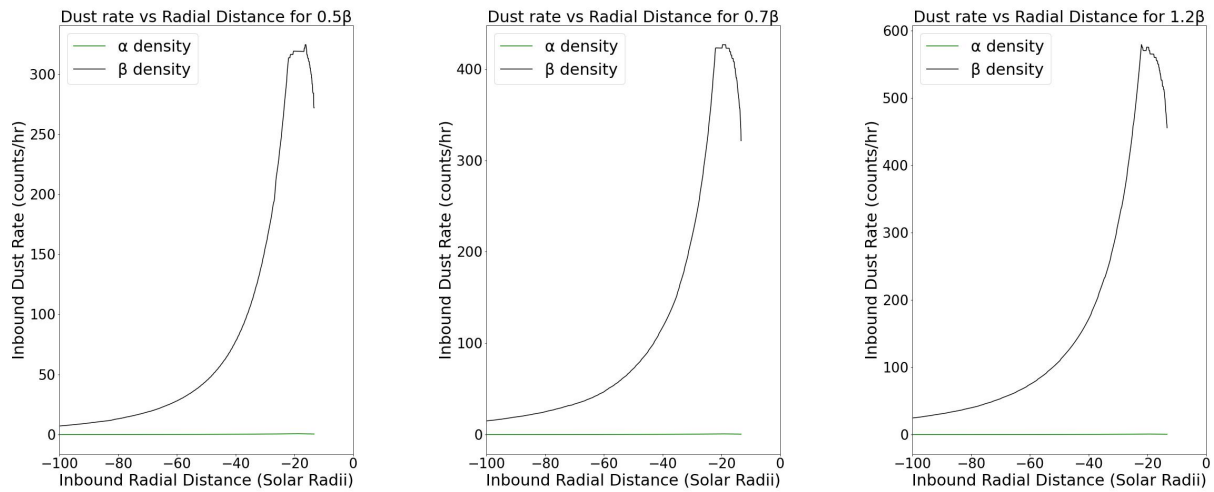
Figure 6.3: Radial distance vs dust rate for α(green line) and β(black line) for differing values of β. from left to right $0.5\beta, 0.7\beta$,and 1.2β. Note that the x-axis is negative in order to illustrate an inbound trajectory of PSP and keep consistency with figures 5.8 and 5.9 *top*. Assume that the radial distance is the magnitude of the x-axis values.
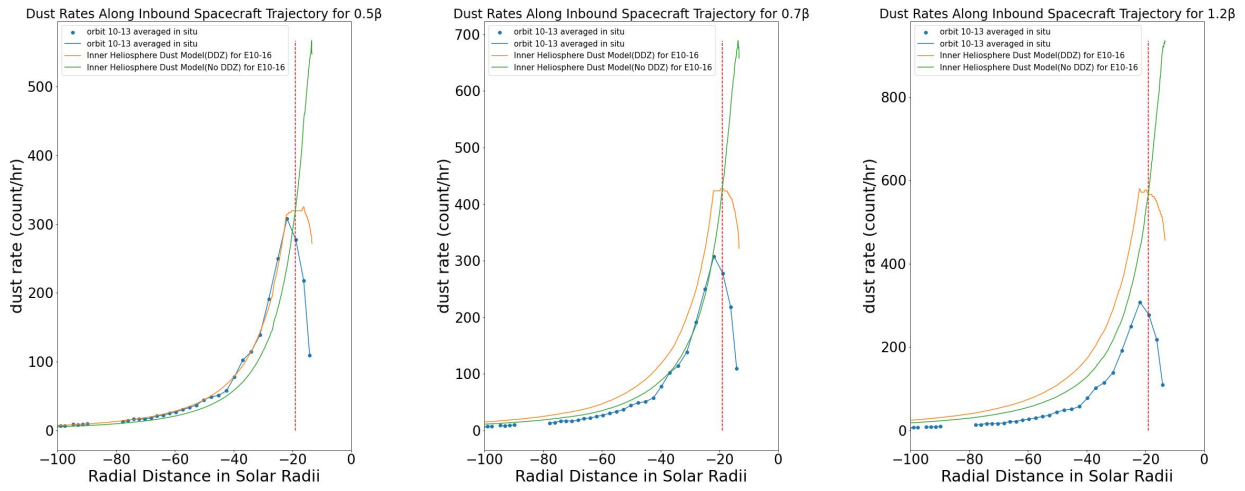
Figure 6.4: Radial distance vs dust rate for: in-situ data from DFB averaged over Encounters 10 through 13 (blue with dots),the Inner Heliosphere Dust Model with DDZ present (orange line), the Inner Heliosphere Dust Model without DDZ (green line) for differing β values. from left to right 0.5β,0.7β,and 1.2β. The red dashed line represents $r = 19R_\odot$, the point at which WISPR states the DDZ begins. Note that the x-axis is negative in order to illustrate an inbound trajectory of PSP and keep consistency with figures 5.8 and 5.9 *top*. Assume that the radial distance is the magnitude of the x-axis values.

Chapter 7

Discussion

A direct comparison between the in-situ measured dust impact rate and Inner Heliosphere Dust Model (see 6.4) has shown that the proposed DDZ theory agrees with the WISPR team's initial modeling (Stenborg et al., 2021). Comparing the models assuming no DDZ, the increased amplitude and sunward shift of the Inner Heliosphere Dust Model count rate shows that there must be a loss of the dust density in the region of $19R_\odot$ to $1R_\odot$.

Initial modeling by the WISPR team determined the DFZ boundary began near $3R_\odot$, but PSP has no planned encounter that close to the sun. Encounter 24, the last one planned, will have a perihelion of $9.86R_\odot$. Therefore, it is hard to confirm using in situ data if the model accurately models the inner boundary of the DDZ and subsequently the outer boundary of the DFZ. As PSP progresses towards its final encounters, we can look for characteristics that indicate the transition between the DDZ and DFZ, but future missions may be necessary to get closer to the sun.

The zodiacal cloud in the inner heliosphere can now be defined as an inhomogeneous body, with decreasing dust density from $19R_\odot$ to $1R_\odot$. Given an initial outer boundary set for dust density depletion, there is an argument to be made of the zodiacal cloud being differently shaped in the center of our solar system than what previous models predicted. It could be that we are seeing a range of dust particles of different compositions in certain regions of the inner heliosphere that gives it the non-rigid boundary structure that we see with the data. This is further echoed in the process by which we determined β meteorites in that region.

The Inner Heliosphere Dust Model comes with a set of assumptions. Firstly, the dust density

vs radial distance model that the WISPR team has produced is in arbitrary units. In the dust rate calculation of the intermediary α and β models, we approximated the best possible value of the density of both α and β meteoroids at 1AU (see Cooke et al. (1993) and Grün et al. (1983)). In addition, we also assumed that the density shape for both α and β meteorites follows the shape of figure 3.4, where the density falls off $1/r^{1.03}$ for α and $1/r^2$ for β. This is an ideal assumption and it yields results close to what we expect, but the zodiacal cloud is not an ideal system. Further exploration of accurate β meteorite dust density in that region must be conducted.

In addition to the model, we saw that the choice of β affects the result directly. We used the three values of β present in figure 6.2. The results of the α and β meteorite densities when computed with each of the β velocities, suggest that our value for $\beta = 0.5$ is the most likely type of β meteorites in the inner heliosphere region. This was a result of averaging the dust rate of each orbit. This is not the case for each orbit modeled individually.
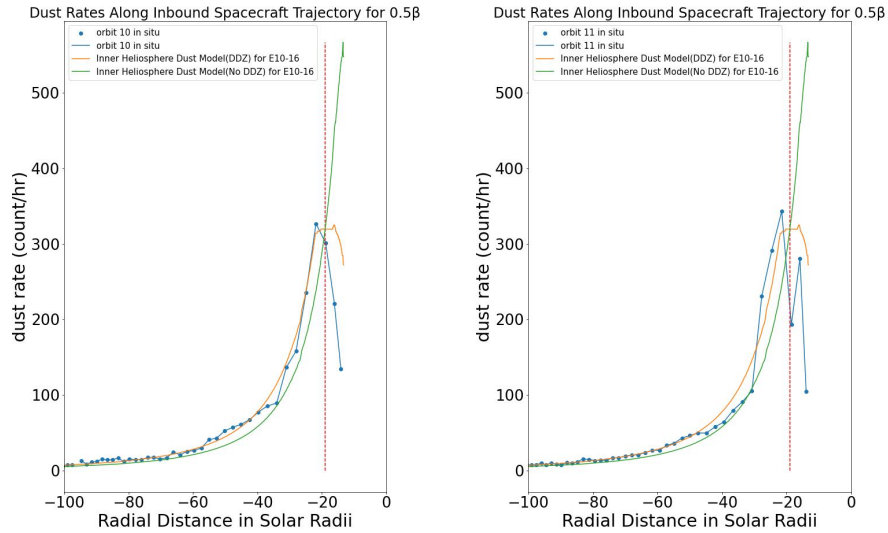
Figure 7.1: Radial distance vs dust rate for: in-situ data from DFB for Encounters 10 and 11 (blue with dots),the Inner Heliosphere Dust Model with DDZ present (orange line), the Inner Heliosphere Dust Model without DDZ (green line) for 0.5β. The red dashed line represents $r = 19R_\odot$, the point at which WISPR states the DDZ begins. Note that the x-axis is negative in order to illustrate an inbound trajectory of PSP and keep consistency with figures 5.8 and 5.9 *top*. Assume that the radial distance is the magnitude of the x-axis values.

On an encounter-by-encounter basis, the data suggests that 0.5β works for regions farther away than $40\text{R}_\odot$ while 0.7β works for the section sunward beginning at $40\text{R}_\odot$. Given that we could scale 0.7β's dust rate to a fraction of the currently shown in the figures, a near identical curve would be present in the inner solar region of $40\text{R}_\odot$ to $1\text{R}_\odot$. Additionally, it is seen that the peak for the Inner Heliosphere Dust Model is positioned slightly closer to the sun compared to the in-situ dust rates. This is likely because of α's minimal effect on the overall shape of the Inner Heliosphere Dust Model curve (as shown in figure 6.3). The boundary conditions of α and β must be calibrated separately to see what effects they have on the overall shape of the Inner Heliosphere Dust Model.

In-situ dust rate measurements in Encounter 13 do not exhibit any of the same characteristics that the other encounters in the group do. Encounter 11 also exhibits erratic characteristics that do not follow Encounters 10 and 12, yet the shape of the data is not so drastic as to cause alarm. This led to a model comparison with the average dust rate over the four encounters vs the DDZ-derived
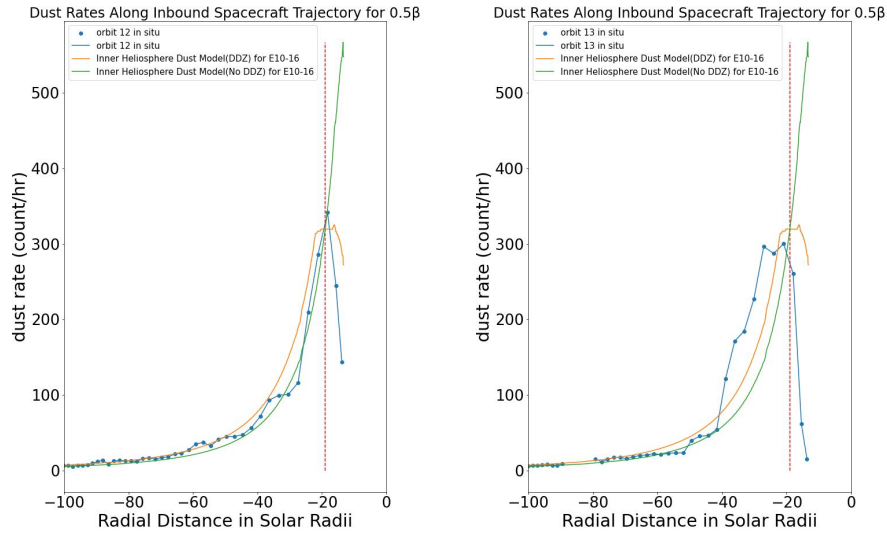
Figure 7.2: Radial distance vs dust rate for: in-situ data from DFB for Encounters 12 and 13 (blue with dots),the Inner Heliosphere Dust Model with DDZ present (orange line), the Inner Heliosphere Dust Model without DDZ (green line) for 0.5β. The red dashed line represents $r = 19\text{R}_\odot$, the point at which WISPR states the DDZ begins. Note that the x-axis is negative in order to illustrate an inbound trajectory of PSP and keep consistency with figures 5.8 and 5.9 *top*. Assume that the radial distance is the magnitude of the x-axis values.

WISPR data, which proved more promising but overall produced a fair amount of uncertainty in our analysis. Further research into Encounter 13 should be conducted, to see if there was any external event or factor that affected data collection.

The shown figures further explain the non-homogeneity of the zodiacal cloud in the inner heliosphere and propose that there are external factors affecting the overall makeup of that region. There are two main arguments can possibly further explain. The first is that there are external objects that pass through the inner heliosphere fragmenting pieces of themselves into the region. The second is that given the elemental composition of the dust particles, certain particles remain in that area with their own set of characteristics, as compared to other particles of a different makeup, which might not resist the environmental conditions of the near sun region. The former might directly affect the latter, but a more in-depth study of the region with a dedicated detector analyzing compositional makeup is needed.
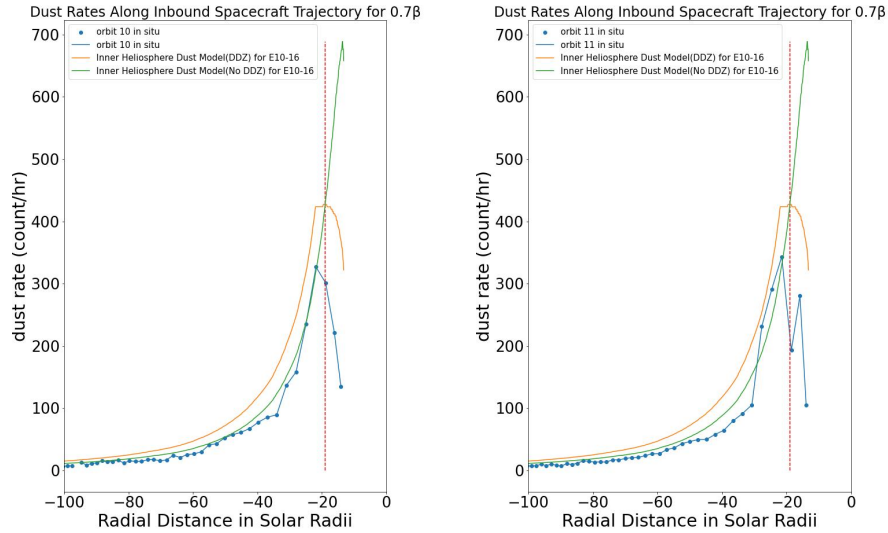
Figure 7.3: Radial distance vs dust rate for: in-situ data from DFB for Encounters 10 and 11 (blue with dots),the Inner Heliosphere Dust Model with DDZ present (orange line), the Inner Heliosphere Dust Model without DDZ (green line) for 0.7β. The red dashed line represents $r = 19\text{R}_\odot$, the point at which WISPR states the DDZ begins. Note that the x-axis is negative in order to illustrate an inbound trajectory of PSP and keep consistency with figures 5.8 and 5.9 *top*. Assume that the radial distance is the magnitude of the x-axis values.
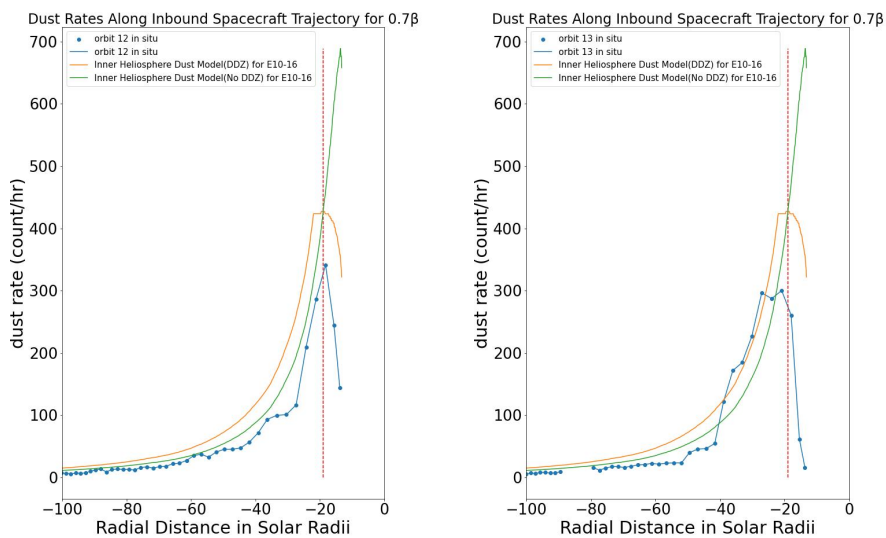
Figure 7.4: Radial distance vs dust rate for: in-situ data from DFB for Encounters 12 and 13 (blue with dots),the Inner Heliosphere Dust Model with DDZ present (orange line), the Inner Heliosphere Dust Model without DDZ (green line) for 0.7β. The red dashed line represents $r = 19R_{\odot}$, the point at which WISPR states the DDZ begins. Note that the x-axis is negative in order to illustrate an inbound trajectory of PSP and keep consistency with figures 5.8 and 5.9 *top*. Assume that the radial distance is the magnitude of the x-axis values.

Chapter 8

Conclusions and Future Work

At the time of writing this paper, PSP has reached its 14th orbital encounter of the sun. The in-situ data analysis and model comparison of count rates that were conducted confirmed the presence of the DDZ. This DDZ is defined with an outer boundary beginning at $19R_\odot$. Although the current Inner Heliosphere Dust Model has directly confirmed the DDZ's existence, more changes can be added to the model to further explore the inner heliosphere region.

Currently, PSP is still within the current orbital group of 10 through 16 that we have used in the analysis. Given that the data shown does not clearly establish the inner boundary of the DDZ and the outer boundary of the DFZ, it is recommended that identical methods applied to the first thirteen orbits should continue to be applied to subsequent orbits. Focusing directly on defining boundary region parameters for both DDZ and DFZ will further explain the inner heliosphere region of the zodiacal cloud.

The code set in place that produces the Inner Heliosphere Dust Model from the WISPR data is allowed to be reconfigured for further testing. An extensive model comparison of in-situ data and the Inner Heliosphere Dust Model, using a multitude of configurations must be held to produce a complete formulation of the DDZ boundary. Furthermore, it should be noted that given the assumptions made in the construction of β WISPR data representation, the WISPR shape might need to be reformed (Stenborg et al., 2021). This should be done if sufficient information regarding β formation and characteristics in the near heliosphere region is found.

As the first of its kind, PSP has managed to give insight into inner heliosphere dust charac-

teristics and interactions. Until now, the zodiacal cloud has only been analytically and numerically approximated to produce its shape. The initial steps of this discovery begin to explore in further detail not only the shape but the non-homogeneity of interstellar dust density in the zodiacal cloud, a region that was unavailable for scientists to explore in detail until now.

Additionally, new questions about interstellar dust interaction arise from this study. A strange event was noticed during the formation of the DFB dust impact database. In this event, dust impacts occur incredibly close to each other on the order of milliseconds. This event was present throughout all of the encounters used. This is not only a strange occurrence to see in the data but is also physically interesting. Particle detection in this close of a time span means that the particles are relatively close to each other. Exploration of questions such as these allows scientists to further explore and understand the interaction between a star and the dust near it. Initial observations may be used to understand larger topics such as dust destruction, and planetary formation as a result of dust particles leaving this region.

One possibility for this event is that we are witnessing soft breakup events of dust particles, where they fragment off and don't have enough time to move far enough away from each other. This is due to extreme weather exposure of interstellar dust in the inner heliosphere region. Thus, when PSP flies through that region in space, we encounter two very close dust impacts. This does not explain the second observation made. That is events occur, on average, more during the inbound trajectory portion of the orbit than on the outbound trajectory. This is strange and could be due to the non-uniformity of the zodiacal cloud. This effect could also occur given the trajectory of movement dust particles experience relative to the spacecraft. This specific region might see particles of dust hitting against the spacecraft, while after perihelion the spacecraft travels along the direction of the dust, thereby seeing less impact occur.

Another proposition is that the compositional elements of the dust are not originally of that region. Instead, we may observe dust that has ejected off an unknown body through sputtering. Those fragments become our β meteorites and pelt PSP. This furthers the question of dust composition of interstellar dust present in the inner heliosphere region. PSP is not enough to further

explore the second proposal, since there is no dedicated dust detector on the spacecraft, nor is there a second spacecraft that can be used to map out dust impact trajectories. It would therefore fall on a future mission to not only go into that region again but also to include a dust detector that allows researchers to look directly at the compositional makeup of those dust particles.

As PSP continues to acquire more data, we must continue to tabulate each dust impact into the standardized database. This will allow scientists to further explain unanswered questions using an established method, further alleviating any case of discrepancy in the measuring and processing method. However, PSP has completed over half of its planned orbits. This means that most of the mission objectives have been fully explained or are still being answered. In addition, scientists and engineers alike will gain a better understanding of how to conduct future missions in this region of space.

The DFZ's existence will now be sought out through a complete modeling of the DDZ. The more we know about the inner region of our solar system, as well as the sun itself, the more scientists will be able to gain a deeper understanding of the formation of our solar system, and engineers will gain insight into the risks of sending a spacecraft this close to the sun. PSP has and will continue to allow researchers to establish a clear theory of how solar systems are formed, how stars interact with their local medium, and the dynamics of interplanetary dust.

Bibliography

L. Andersson, T. D. Weber, D. Malaspina, F. Crary, R. E. Ergun, G. T. Delory, C. M. Fowler, M. W. Morooka, T. McEnulty, A. I. Eriksson, D. J. Andrews, M. Horanyi, A. Collette, R. Yelle, and B. M. Jakosky. Dust observations at orbital altitudes surrounding Mars. Science, 350(6261): 0398, Nov. 2015. doi: 10.1126/science.aad0398.

S. D. Bale, K. Goetz, P. R. Harvey, P. Turin, J. W. Bonnell, T. Dudok de Wit, R. E. Ergun, R. J. MacDowall, M. Pulupa, M. Andre, M. Bolton, J. L. Bougeret, T. A. Bowen, D. Burgess, C. A. Cattell, B. D. G. Chandran, C. C. Chaston, C. H. K. Chen, M. K. Choi, J. E. Connerney, S. Cranmer, M. Diaz-Aguado, W. Donakowski, J. F. Drake, W. M. Farrell, P. Fergeau, J. Fermin, J. Fischer, N. Fox, D. Glaser, M. Goldstein, D. Gordon, E. Hanson, S. E. Harris, L. M. Hayes, J. J. Hinze, J. V. Hollweg, T. S. Horbury, R. A. Howard, V. Hoxie, G. Jannet, M. Karlsson, J. C. Kasper, P. J. Kellogg, M. Kien, J. A. Klimchuk, V. V. Krasnoselskikh, S. Krucker, J. J. Lynch, M. Maksimovic, D. M. Malaspina, S. Marker, P. Martin, J. Martinez-Oliveros, J. McCauley, D. J. McComas, T. McDonald, N. Meyer-Vernet, M. Moncuquet, S. J. Monson, F. S. Mozer, S. D. Murphy, J. Odom, R. Oliverson, J. Olson, E. N. Parker, D. Pankow, T. Phan, E. Quataert, T. Quinn, S. W. Ruplin, C. Salem, D. Seitz, D. A. Sheppard, A. Siy, K. Stevens, D. Summers, A. Szabo, M. Timofeeva, A. Vaivads, M. Velli, A. Yehle, D. Werthimer, and J. R. Wygant. The FIELDS Instrument Suite for Solar Probe Plus. Measuring the Coronal Plasma and Magnetic Field, Plasma Waves and Turbulence, and Radio Signatures of Solar Transients. , 204(1-4):49–82, Dec. 2016. doi: 10.1007/s11214-016-0244-5.

W. J. Cooke, J. D. Mulholland, and J. P. Oliver. IDE constraints on the beta meteoroid population. Advances in Space Research, 13(8):119–122, Aug. 1993. doi: 10.1016/0273-1177(93)90577-X.

N. J. Fox, M. C. Velli, S. D. Bale, R. Decker, A. Driesman, R. A. Howard, J. C. Kasper, J. Kinnison, M. Kusterer, D. Lario, M. K. Lockwood, D. J. McComas, N. E. Raouafi, and A. Szabo. The Solar Probe Plus Mission: Humanity's First Visit to Our Star. , 204(1-4):7–48, Dec. 2016. doi: 10.1007/s11214-015-0211-6.

E. Grün, H. A. Zook, and H. Fechtig. Collisional balance of the meteoritic complex. Uppsala Astronomical Observatory Reports, 25:36, Jan. 1983.

D. A. Gurnett, E. Grun, D. Gallagher, W. S. Kurth, and F. L. Scarf. Micron-sized particles detected near Saturn by the Voyager plasma wave instrument. , 53(2):236–254, Feb. 1983. doi: 10.1016/0019-1035(83)90145-8.

J. C. Kasper, R. Abiad, G. Austin, M. Balat-Pichelin, S. D. Bale, J. W. Belcher, P. Berg, H. Bergner, M. Berthomier, J. Bookbinder, E. Brodu, D. Caldwell, A. W. Case, B. D. G.

Chandran, P. Cheimets, J. W. Cirtain, S. R. Cranmer, D. W. Curtis, P. Daigneau, G. Dalton, B. Dasgupta, D. DeTomaso, M. Diaz-Aguado, B. Djordjevic, B. Donaskowski, M. Effinger, V. Florinski, N. Fox, M. Freeman, D. Gallagher, S. P. Gary, T. Gauron, R. Gates, M. Goldstein, L. Golub, D. A. Gordon, R. Gurnee, G. Guth, J. Halekas, K. Hatch, J. Heerikuisen, G. Ho, Q. Hu, G. Johnson, S. P. Jordan, K. E. Korreck, D. Larson, A. J. Lazarus, G. Li, R. Livi, M. Ludlam, M. Maksimovic, J. P. McFadden, W. Marchant, B. A. Maruca, D. J. McComas, L. Messina, T. Mercer, S. Park, A. M. Peddie, N. Pogorelov, M. J. Reinhart, J. D. Richardson, M. Robinson, I. Rosen, R. M. Skoug, A. Slagle, J. T. Steinberg, M. L. Stevens, A. Szabo, E. R. Taylor, C. Tiu, P. Turin, M. Velli, G. Webb, P. Whittlesey, K. Wright, S. T. Wu, and G. Zank. Solar Wind Electrons Alphas and Protons (SWEAP) Investigation: Design of the Solar Wind and Coronal Plasma Instrument Suite for Solar Probe Plus. , 204(1-4):131–186, Dec. 2016. doi: 10.1007/s11214-015-0206-3.

D. Koschny, R. H. Soja, C. Engrand, G. J. Flynn, J. Lasue, A.-C. Levasseur-Regourd, D. Malaspina, T. Nakamura, A. R. Poppe, V. J. Sterken, and J. M. Trigo-Rodríguez. Interplanetary Dust, Meteoroids, Meteors and Meteorites. , 215(4):34, June 2019. doi: 10.1007/s11214-019-0597-7.

W. S. Kurth, T. F. Averkamp, D. A. Gurnett, and Z. Wang. Cassini RPWS observations of dust in Saturn's E Ring. , 54(9-10):988–998, Aug. 2006. doi: 10.1016/j.pss.2006.05.011.

H. Laakso, R. Grard, A. Pedersen, and G. Schwehm. Impacts of large dust particles on the Vega spacecraft. Advances in Space Research, 9(3):269–272, Jan. 1989. doi: 10.1016/0273-1177(89) 90273-1.

R. A. London and J. T. Early. Evaluation of the hazard of dust impacts on interstellar spacecraft. Journal of the British Interplanetary Society, 71(4), 4 2018.

D. Malaspina, A. Toma, J. R. Szalay, M. Pulupa, P. Pororny, S. D. Bale, and K. Goetz. A dust detection database for the inner heliosphere using the Parker Solar Probe spacecraft (Under Review). The Astrophysical Journal Supplement, 2023.

D. M. Malaspina, M. Horányi, A. Zaslavsky, K. Goetz, L. B. Wilson, and K. Kersten. Interplanetary and interstellar dust observed by the Wind/WAVES electric field instrument. , 41(2):266–272, Jan. 2014. doi: 10.1002/2013GL058786.

D. M. Malaspina, R. E. Ergun, M. Bolton, M. Kien, D. Summers, K. Stevens, A. Yehle, M. Karlsson, V. C. Hoxie, S. D. Bale, and K. Goetz. The Digital Fields Board for the FIELDS instrument suite on the Solar Probe Plus mission: Analog and digital signal processing. Journal of Geophysical Research (Space Physics), 121(6):5088–5096, June 2016. doi: 10.1002/2016JA022344.

I. Mann. Evolution of Dust and Small Bodies: Physical Processes, pages 1–42. Springer Berlin Heidelberg, Berlin, Heidelberg, 2009. ISBN 978-3-540-76935-4. doi: 10.1007/978-3-540-76935-4_7. URL https://doi.org/10.1007/978-3-540-76935-4_7.

D. J. McComas, N. Alexander, N. Angold, S. Bale, C. Beebe, B. Birdwell, M. Boyle, J. M. Burgum, J. A. Burnham, E. R. Christian, W. R. Cook, S. A. Cooper, A. C. Cummings, A. J. Davis, M. I. Desai, J. Dickinson, G. Dirks, D. H. Do, N. Fox, J. Giacalone, R. E. Gold, R. S. Gurnee, J. R. Hayes, M. E. Hill, J. C. Kasper, B. Kecman, J. Klemic, S. M. Krimigis, A. W. Labrador, R. S. Layman, R. A. Leske, S. Livi, W. H. Matthaeus, R. L. McNutt, R. A. Mewaldt, D. G. Mitchell, K. S. Nelson, C. Parker, J. S. Rankin, E. C. Roelof, N. A. Schwadron, H. Seifert, S. Shuman,

M. R. Stokes, E. C. Stone, J. D. Vandegriff, M. Velli, T. T. von Rosenvinge, S. E. Weidner, M. E. Wiedenbeck, and P. Wilson. Integrated Science Investigation of the Sun (ISIS): Design of the Energetic Particle Investigation. , 204(1-4):187–256, Dec. 2016. doi: 10.1007/s11214-014-0059-1.

N. Meyer-Vernet, M. Maksimovic, A. Czechowski, I. Mann, I. Zouganelis, K. Goetz, M. L. Kaiser, O. C. St. Cyr, J. L. Bougeret, and S. D. Bale. Dust Detection by the Wave Instrument on STEREO: Nanoparticles Picked up by the Solar Wind? , 256(1-2):463–474, May 2009. doi: 10.1007/s11207-009-9349-2.

H. N. Russell. On Meteoric Matter Near the Stars. , 69:49, Jan. 1929. doi: 10.1086/143158.

G. Stenborg, R. A. Howard, P. Hess, and B. Gallagher. PSP/WISPR observations of dust density depletion near the Sun. I. Remote observations to 8 $R_\odot$ from an observer between 0.13 and 0.35 AU. , 650:A28, June 2021. doi: 10.1051/0004-6361/202039284.

J. R. Szalay, P. Pokorný, S. D. Bale, E. R. Christian, K. Goetz, K. Goodrich, M. E. Hill, M. Kuchner, R. Larsen, D. Malaspina, D. J. McComas, D. Mitchell, B. Page, and N. Schwadron. The Near-Sun Dust Environment: Initial Observations from Parker Solar Probe. , 246(2):27, Feb. 2020. doi: 10.3847/1538-4365/ab50c1.

B. T. Tsurutani, D. R. Clay, L. D. Zhang, B. Dasgupta, D. Brinza, M. Henry, J. K. Arballo, S. Moses, and A. Mendis. Plasma clouds associated with Comet P/Borrelly dust impacts. , 167 (1):89–99, Jan. 2004. doi: 10.1016/j.icarus.2003.08.021.

J. Vaverka, J. Pavlu, J. Safrankova, Z. Nemecek, I. Mann, M. Hamrin, and A. Pellinen-Wannberg. Dust impacts detection by multiple electric field antennas, signal interpretation. In EGU General Assembly Conference Abstracts, EGU General Assembly Conference Abstracts, page 4822, Apr. 2018.

A. Vourlidas, R. A. Howard, S. P. Plunkett, C. M. Korendyke, A. F. R. Thernisien, D. Wang, N. Rich, M. T. Carter, D. H. Chua, D. G. Socker, M. G. Linton, J. S. Morrill, S. Lynch, A. Thurn, P. Van Duyne, R. Hagood, G. Clifford, P. J. Grey, M. Velli, P. C. Liewer, J. R. Hall, E. M. DeJong, Z. Mikic, P. Rochus, E. Mazy, V. Bothmer, and J. Rodmann. The Wide-Field Imager for Solar Probe Plus (WISPR). , 204(1-4):83–130, Dec. 2016. doi: 10.1007/s11214-014-0114-y.

A. Zaslavsky, N. Meyer-Vernet, I. Mann, A. Czechowski, K. Issautier, G. Le Chat, F. Pantellini, K. Goetz, M. Maksimovic, S. D. Bale, and J. C. Kasper. Interplanetary dust detection by radio antennas: Mass calibration and fluxes measured by STEREO/WAVES. Journal of Geophysical Research (Space Physics), 117(A5):A05102, May 2012. doi: 10.1029/2011JA017480.

H. A. Zook and O. E. Berg. A source for hyperbolic cosmic dust particles. , 23(1):183–203, Jan. 1975. doi: 10.1016/0032-0633(75)90078-1.